Broadband single and multimode quantum light generation using optical nonlinearities

by

Sahil Pontula

S.B., Massachusetts Institute of Technology (2023)

Submitted to the Department of Electrical Engineering and Computer Science

in partial fulfillment of the requirements for the degree of

Master of Science

at the

MASSACHUSETTS INSTITUTE OF TECHNOLOGY

May 2024

Authored by: Sahil Pontula
Department of Electrical Engineering and Computer Science
May 17, 2024

Certified by: Marin Soljačić
Professor of Physics
Thesis Supervisor

Accepted by: Leslie A. Kolodziejski
Professor of Electrical Engineering and Computer Science
Chair, Department Committee on Graduate Students

Broadband single and multimode quantum light generation using optical nonlinearities

by

Sahil Pontula

Submitted to the Department of Electrical Engineering and Computer Science
on May 17, 2024, in partial fulfillment of the
requirements for the degree of
Master of Science

Abstract

There is a growing effort in many fields of physics to bridge the classical and quantum realms. To our best understanding, our world is governed by the laws of quantum mechanics, but some of its most interesting features - such as the ability to morph uncertainty and noise - are washed out when system sizes become too large. Light is the ideal playground to investigate the interplay between the classical and quantum domains, with its well known particle-wave duality and diverse behaviors at both the classical wave and single photon levels. To this end, there is significant interest in generating quantum states of light that can be harnessed for applications in the classical world we are most familiar with. However, maintaining "quantumness" as the number of photons grows large has proved challenging due to the detrimental effects of loss. In this thesis, I describe two theoretical proposals to make macroscopic quantum light a reality. I focus on bright intensity squeezed states of light that have intensity noise far below the standard quantum limit. If realized, these states would bring the quantum mechanical phenomenon of squeezing to macroscopic intensities, which in turn could pave the way towards widespread quantum light sources that offer enhanced signal to noise ratios. I describe two distinct methods that use tools from nonlinear optics and dissipation engineering to realize broadband squeezing in both single and multiple frequency modes. I show that the squeezing can be tunable across a wide range of the electromagnetic spectrum that spans frequencies where quantum light has never been generated.

Thesis Supervisor: Marin Soljačić
Title: Professor of Physics

Acknowledgments

I acknowledge my current faculty advisor, Marin Soljačić, as well as my collaborators and mentors so far, Yannick Salamin, Jamison Sloan, and Nick Rivera, for their guidance along my journey exploring nonlinear and quantum optics. I would also like to thank my other research supervisors, John Simonaitis, Phiala Shanahan, and Dan Hackett, for their advice as I navigated my interests at the intersection of physics and engineering. Going further back, I thank my former research mentors, Peter Lu and Abhichart Krissanaprasit, with whom I worked starting in high school, as well as Hamidreza Akbari, Pankaj Jha, and Harry Atwater, with whom I worked during Summer 2021 at Caltech. Their incredible guidance kept my spark of curiosity and innovation going and exposed me to diverse research disciplines. This work would also not be possible without the financial support of the National Science Foundation and Hertz Fellowship Foundation. Lastly, I thank my family for their unfailing support through everything.

Contents

List of Figures

3-3 **Single and multimode output noise squeezing.** (a) Using a similar cavity design to that presented in Fig. 3-2, single frequency modes in the synthetic frequency dimension can be squeezed in output noise. Here, we simulate $N = 15$ cascading orders, and the mode with low Q is squeezed. Dashed lines demarcate the boundaries of the frequency space cavity. We plot the steady state output power in the modes; due to their low Q, the squeezed modes have the highest power outside the cavity. The remaining IR modes show an interference pattern in steady state power characteristic of the Bloch interference phenomenon in Fig. 3-2. The terahertz mode a_T also has high power, while modes outside the frequency space cavity are very leaky and negligibly occupied in the steady state. The modes that are designed to have low Q are the only ones to show significant departure from the shot noise limit (SNL), demonstrating intensity noise squeezing exceeding 10 dB. In these simulations, $Q_0 = 3 \times 10^6, Q_N = 2 \times 10^5, Q_r = Q_T = 10^9$ and $\kappa = 14.1$ s^{-1}. (b), (c) The single mode output squeezing (here for mode a_N) can be maximized by optimizing multiple parameters simultaneously. Here, we show that higher Q_T and lower intrinsic loss generates stronger squeezing due to stronger nonlinear energy flow. A larger number of modes (N) can also help increase squeezing, though too many modes can make the noise contribution from modes $a_{k\neq N}$ significant (red dashed curve in (c)). Lastly, an optimal Q_N exists (with all parameters held equal) to maximize squeezing. Roughly, this Q_N maximizes destructive interference with vacuum shot noise as per condition (1) (red dotted curve in (c)). In (b), (c), $Q_r = 10^8$ and μ/γ denotes the ratio of intrinsic loss to the outcoupling rate. (d), (e) By shaping the Q factor profile of the multimode cavity, specifically by introducing multiple Q factor "defects," output squeezing can be obtained for multiple frequency modes. Here, $N = 7$ modes are simulated. The bandwidth for squeezing in the inset is around 100 MHz, but can be optimized to > 1 GHz by enabling stronger nonlinear rates. 65

A-4 **Effects of carrier and Kerr nonlinearities composed with dispersive loss**. (a) In the presence of only carrier nonlinearity σ, the resonance frequency and thus loss depend "directly" on carrier density N, and steady states are set by the intersections of gain and loss. For strong σ and low background loss κ_0, multiple steady state carrier densities N can correspond to a given photon number n, resulting in different steady state losses (detunings from the Fano resonance). The lowest loss solution (smallest detuning) is most likely to lase, though extra solutions may be accessible by dynamic pumping schemes. (b) The schematic effect of this "carrier bistability" is to create multiple branches in the S-curve of different slope/threshold current. The presence of both strong carrier and Kerr nonlinearities result in the novel behaviors shown in panels (c), (d), and (e). Carrier nonlinearity causes a deformation of the intensity-nonlinear Lorentzian loss profile, eventually pinching off the "sharp loss" from the linear loss for sufficiently strong carrier nonlinearity (purple curve). This stems from leftward motion of the carrier bistability boundaries and creates a demarcation between linear ($F \gg 1$) and nonlinear ($F < 1$) loss regimes which may be separated by a region of lasing with no stable solution. System parameters used are the same as those in Fig. 2 with $\beta = -10^{-10}$, $\kappa_0 = 10^{-2} \cdot \mathrm{FSR}$, and $\gamma = 2 \times 10^{12}$ rad/s. The magnitudes of Kerr and carrier nonlinearities taken here are comparable to what they might be in GaAs-based gain media: $\beta \sim -10^{-10}$ and $\sigma \sim -3 \times 10^{-27}$ m^3 (with the proviso of being taken as instantaneous and being evaluated at a single wavelength). 94

List of Tables

Chapter 1

Introduction

The generation of quantum states of light is a long-standing goal of quantum optics. These states comprise a toolbox from which quantum mechanical properties such as squeezing and entanglement can be harnessed to enhance the performance of classical photonic devices. The past few years have seen a burgeoning interest in research towards realizing practical sources of quantum light, driven largely by quantum computing but also by sensing and metrology applications (e.g., the use of squeezed vacuum by the LIGO gravitational wave detector). Despite this incredible progress, there are some quantum states of light that still remain notoriously elusive despite their tantalizing potential for real-world applications. Examples include many-photon Fock states (which have no photon number uncertainty) and macroscopic states of light (states such as those in optical cavities like lasers) with strongly squeezed intensity noise. (When the squeezing is infinite, a macroscopic Fock state is produced.) The main issue is loss, though most existing protocols to generate bright squeezing also suffer from low bandwidths and lack spectral tunability. For example, protocols to produce quantum light at some frequencies (e.g., microwave) do not easily generalize to other frequencies (e.g., optical). In this thesis, I describe two theory projects that aim to harness loss and optical nonlinearity in ways that are advantageous for squeezing - first by engineering nonlinear dissipation to create strong single-mode squeezing and second by controlling the relationship between outcoupling loss and nonlinear intermodal coupling to generate multimode output

squeezing. These works pave the way towards single-mode and multimode sources of bright intensity noise-squeezed states of light that could provide a new resource for multiple quantum applications, such as on-demand squeezed light generation from lasers and squeezed frequency combs for metrology applications.

Chapter 2 describes my theoretical proposal for generating strong intensity noise squeezing (both intracavity and output) in semiconductor lasers. As I show, through a combination of Kerr nonlinearity and photonic crystal-based dispersive loss, semiconductor laser systems can be engineered to have sharply nonlinear intensity-dependent dissipation, resulting in strongly squeezed steady states. Using quantum cascade laser architectures, nonlinear dissipation can extend strong squeezing to frequency ranges that have not been previously investigated for quantum light generation, such as the mid-infrared (mid-IR) and terahertz (THz). Furthermore, I show how the same phenomenon of nonlinear dissipation creates bistability and diverse mean field behaviors, including picosecond self-pulsing. Together, these results may enable combined dynamical and quantum noise control across a wide range of wavelengths in a single semiconductor laser platform.

In Chapter 3, I describe my work over the past academic year demonstrating multimode squeezing and quantum noise correlations in a platform that supports cascaded second-order nonlinear processes. By controlling the Q factor of different modes in a multimode cavity that are coupled nonlinearly to one another through a common "idler" bath mode, I show how tunable frequency combs and cavities in a synthetic frequency dimension can be created. Within these frequency space cavities, strong nonlinear rates can exceed dissipation rates, resulting in intensity noise squeezing for one or more modes. Furthermore, these strong nonlinear interactions also sustain long-range quantum noise correlations in the synthetic frequency dimension, providing a resource for multimode entanglement.

Finally, in Chapter 4, I describe active projects that I am currently working on, including other theory projects and a free-space experiment designed to demonstrate some of the predictions highlighted in the multimode work above.

Chapter 2

Single mode squeezing in semiconductor lasers at mid-infrared and terahertz frequencies

The content of this chapter is taken largely from my first author preprint [5]. The foundational theory was also developed in my bachelor's thesis [6].

2.1 Introduction

The generation of states of light with noise "squeezed" below the standard quantum limit for a coherent state is a decades-old pursuit of quantum optics. In these squeezed states, the variance in one observable (such as amplitude or phase) is reduced at the expense of another, permitting levels of quantum fluctuations which lie below the standard quantum limit. Such squeezed states of light have been harnessed for optical quantum computing as well as precision sensing and metrology [7, 8]. The most common methods to generate squeezed light employ laser-pumped nonlinear crystals. For example, sub-threshold optical parametric amplifiers have been used to produce up to 3 dB of intracavity squeezing [9–11] and 15 dB of propagating squeezed vacuum [12–14].

By contrast, schemes to generate squeezing in bright states of light are less ma-

ture, despite their promise as sources for sensitive spectroscopy applications and pumps for low-noise optical amplifiers [15, 16]. Generation of bright squeezing has been limited to methods developed over two decades ago such as second harmonic generation, Kerr nonlinearity in fiber-optic interferometers, and "quietly pumped" semiconductor lasers [17–19]. However, these mechanisms come with inherent trade-offs that limit the space of possible applications. First, the magnitude of squeezing achieved has not approached that achievable with squeezed vacuum (in either intracavity or output intensity noise), limiting applications where intense squeezed light is preferred over squeezed vacuum. Secondly, large (GHz) bandwidths have not been demonstrated with these bright squeezing methods, limiting their application in quantum communication protocols. In mesoscopic systems with strong nonlinearities, high levels of broadband intracavity squeezing could produce approximate large Fock states, with exciting potential applications in qubit nondemolition readout in cavity QED, optomechanical cooling, quantum metrology, and enhanced light-matter interactions [11, 20–23]. Finally, existing methods to produce intense squeezed states have been generally limited to narrow wavelength ranges in the infrared (e.g., due to nonlinear phase matching and conversion efficiency constraints). As a result, there are large wavelength ranges (MIR-THz) in which intensity squeezing has never been demonstrated, despite tantalizing applications in quantum-enhanced chemical fingerprinting, wireless communication, and solid-state qubit manipulation [24].

These wavelengths spanning from the IR to the THz have been particularly well-served by semiconductor lasers, owing to their wide gain bandwidths, convenient form factors, and ease of electrical pumping. Several methods have been explored to produce intensity squeezing directly from semiconductor lasers, including so-called "quiet pumping" (pump noise suppression) and optical feedback/dispersive loss to exploit amplitude-phase correlations [25–27]. However, these methods have achieved only a few dB of squeezing. Moreover, such squeezing has been achieved only at low noise frequencies, leaving the large excess noise from so-called "relaxation oscillations" at higher frequencies unmitigated. Thus, the majority of modern semiconductor lasers do not surpass — or even reach — the shot noise limit at large bandwidths. This,

together with the limitations of other nonlinear optical techniques described above, highlights a broad open challenge in producing sources of highly squeezed intense light which are versatile in wavelength and bandwidth.

Here, we show how semiconductor lasers equipped with Kerr nonlinearity and frequency-dependent outcoupling can enable sharply nonlinear dissipation and act as a source of intense squeezed light from IR to THz wavelengths, reducing intracavity fluctuations to more than 10 dB below the shot noise limit. Output fluctuations are significantly suppressed relative to conventional semiconductor lasers and, when combined with quiet pumping schemes, can be squeezed over 10 dB below the shot noise limit at GHz bandwidths. Our approach exploits intensity-dependent dissipation, in conjunction with a semiconductor gain medium, to create a laser architecture which natively produces light with intensity fluctuations far below the shot noise limit. We show that semiconductor laser architectures are aptly suited for this purpose due to their compact form factor, strong intrinsic optical nonlinearities, and ease of on-chip integration with the low loss resonators and photonic crystals required to generate frequency-dependent dissipation. In addition, we explain how these same architectures can exhibit classical nonlinear phenomena such as self-pulsing and bistability. Together, these functionalities could pave the way towards combined temporal and quantum noise control over light across the electromagnetic spectrum. This could unlock elusive quantum states such as THz pulsed squeezed states, with novel applications in communications and sensing.

2.2 Theory

2.2.1 Nonlinear dispersive loss

We first describe how, under the right conditions, the combination of Kerr nonlinearity and frequency-dependent loss lead to a laser cavity with an effective *intensity-dependent loss* that controls the quantum state of light produced by the laser. Consider the cavity architecture shown for a semiconductor laser in Fig. 2-1a. We focus

on a single cavity mode, with annihilation operator a. As is well known, a cavity containing a Kerr nonlinearity develops an intensity-dependent resonance frequency due to the intensity-dependent index of the Kerr material [28]. In the case of semiconductor lasers, free carrier nonlinearities (Fig. 2-1b) also shift the cavity resonance. Then, the cavity resonance frequency depends linearly on the photon number and inverted carrier density n and N as

$$\omega_R(n, N) = \omega_0 \cdot (1 + \beta n + \sigma N), \tag{2.1}$$

as derived in the Appendix. This form for the cavity resonance shift due to semiconductor nonlinearities has been analyzed previously using coupled mode theory and supported experimentally [29–32]. Here, ω_0 is the bare resonance frequency of the cavity mode a, β is a dimensionless per-photon nonlinearity that can be directly calculated from the Kerr nonlinear coefficient n_2 or nonlinear susceptibility $\chi^{(3)}$, and the carrier nonlinearity σ is material-dependent and is directly related to the linewidth enhancement factor (see Appendix for details).

Additionally, in the laser cavity of Fig. 2-1a, one of the end facets is a broadband reflector, while the other is a sharply dispersive element, such as a Fano resonance structure or a Bragg reflector, which equips the cavity with sharply frequency-dependent dissipation through its reflection coefficient $R(\omega)$. When combined, the intensity-dependent resonance frequency and frequency-dependent dissipation give the cavity mode an effective *intensity-dependent dissipation*, which can promote the formation of quantum states [33, 34]. The one critical assumption for this description is that the temporal response of the dispersive mirror is fast compared to the round trip time of the cavity. This corresponds to an adiabatic limit where the dispersive resonance, which sets the cavity transmission $T(\omega)$, is able to near-instantaneously follow shifts in the cavity frequency caused by the nonlinearities. When these assumptions are fulfilled, the cavity field is subject to an effective intensity-dependent

damping rate

$$\begin{aligned}\kappa(n,N) \equiv \kappa(\omega_R(n,N)) &= -\mathrm{FSR}\cdot\log R(\omega_R(n,N)) \\ &\approx \mathrm{FSR}\cdot T(\omega_R(n,N)),\end{aligned} \tag{2.2}$$

where the approximation holds when $R(\omega_R) \approx 1$. Sharply frequency-dependent reflectivity profiles enable the dissipation rate $\kappa(n,N)$ to take on forms which are highly nonperturbative in n, making this type of nonlinear dissipation fundamentally different than the types of nonlinear dissipation realized by multi-photon absorption. One example of such a reflectivity profile has been realized in self-pulsing Fano lasers [1] with low mode volumes which, when augmented with a Kerr nonlinear material (Fig. 2-1c), could create strongly nonlinear dissipation. As we will show, systems exhibiting this kind of loss can provide new behaviors not just in their steady states, but also through new quantum noise behaviors.

Note that in Fig. 2-1a we consider a semiconductor laser with separate gain and Kerr nonlinear elements. We choose to use a different material for the Kerr nonlinearity in order to avoid possible dispersive resonant effects of optical nonlinearity near transition energies in the gain material. The Kerr material is chosen to be a GaAs-based semiconductor due to its strong optical nonlinearity from bound carriers. Semiconductor lasers with nonlinear dispersive loss based on "active nonlinearity" (in which the gain and Kerr materials are the same) may be possible, but the timescale of resonant effects may call into question the adiabatic assumption of the cavity resonance frequency's instantaneous response to changes in photon number, thus placing such systems outside the scope of the models we consider here.

2.2.2 Laser dynamics

Semiconductors typically fall into the category of so-called "class B" lasers, in which the polarization dynamics decay quickly relative to the timescales associated with carrier recombination and cavity decay. In this case, the polarization dynamics are adiabatically eliminated, resulting in Heisenberg-Langevin equations for photon num-

ber and carrier number operators, as derived in the Appendix [2, 35]:

$$\dot{n} = (G(n,N) - \kappa(n,N))\, n + F_n \tag{2.3a}$$

$$\dot{N} = I - \left(nG(n,N) + \gamma_{\|} N\right) + F_N. \tag{2.3b}$$

To be maximally general here, we allow the gain G and loss κ to depend on both the carrier density N and photon number n (the latter could account for gain saturation). In writing this form of the gain and loss, we have assumed that the gain and loss respond effectively instantaneously to changes in the photon and carrier number. Pumping is performed by carrier injection using current I (in units of carrier density per unit time), and $\gamma_{\|}$ denotes the nonradiative decay rate of carriers. The case of optically pumped excitation of free carriers is described in the Appendix. Finally, the decay rates and pump noise are associated with zero-mean Langevin force terms $F_{n,N,}$ with nonzero correlators provided in the Appendix.

In all examples presented in the main text, we consider linear gain which neglects saturation effects, so that $G(n,N) = G(N) = G_N(N - N_{\text{trans}})$ with N_{trans} the transparency carrier density. We found no phenomenological differences using logarithmic quantum well gain or including the effects of gain saturation [36].

2.2.3 Noise properties

The noise properties of semiconductor lasers can be computed by considering operator valued fluctuations of the Heisenberg-Langevin equations from their mean field solutions. In the steady state, this results in a pair of coupled linear equations for the operator values fluctuations δn and δN, which are given as:

$$\begin{bmatrix} \delta\dot{n} \\ \delta\dot{N} \end{bmatrix} = \begin{bmatrix} -n\kappa_n & n\,(G_N - \kappa_N) \\ -G_0 & -(nG_N + \gamma_{\|}) \end{bmatrix} \begin{bmatrix} \delta n \\ \delta N \end{bmatrix} + \begin{bmatrix} F_n - n\kappa_\omega F_\phi \\ F_N \end{bmatrix}. \tag{2.4}$$

Here, $\kappa_n \equiv \partial\kappa/\partial n = -\beta\omega_0\kappa_\omega = -\beta\omega_0(\partial\kappa/\partial\omega)$ represents the sharpness of the dispersive loss, $\kappa_N \equiv \partial\kappa/\partial N = \alpha_L G_N \kappa_\omega/2 = -\sigma\omega_0\kappa_\omega$, where α_L is the linewidth enhance-

ment factor (directly related to σ, the free carrier dependence of the refractive index), and F_ϕ is a Langevin force associated with the phase equation of motion. Note that α_L, which emerges due to amplitude-phase coupling in semiconductor lasers, affects noise behavior, but not steady state operation. Important physical parameters to characterize intensity noise are the relaxation oscillation frequency and damping rate of relaxation oscillations. As derived in the Appendix, these can be calculated from the complex poles of the fluctuation dynamics:

$$\begin{aligned} \Omega_R^2 &\approx (nG_N + \gamma_\parallel)(n\kappa_n) + n(G_N - \kappa_N)\kappa \\ \Gamma_1 &\approx n(G_N + \kappa_n) + \gamma_\parallel. \end{aligned} \tag{2.5}$$

These measures provide an important way to understand the effect of nonlinear dispersive loss on quantum noise. They will also dictate mean field dynamics that result from fluctuations from steady state operation.

Going forward, we will assume in the main text that the shift in refractive index due to Kerr nonlinearity is much stronger than that due to carrier nonlinearity, $|\beta n| \gg |\sigma(N - N_{\text{trans}})|$, so that the dependence of loss on carrier number κ_N can be neglected. With strong Kerr nonlinearity, this is generally true for linewidth enhancement factors $\alpha_L < 5$. Many semiconductor laser systems fall in this regime, but quantum well/quantum dot designs and gain-symmetric quantum cascade lasers generally minimize α_L [37,38]. We consider the behavior when $|\beta n| \sim |\sigma(N - N_{\text{trans}})|$ as well as the effect of two photon absorption in the Appendix.

2.3 Results

2.3.1 Mean-field dynamics

We begin by considering the mean-field steady-state and dynamical solutions that emerge for a Kerr nonlinear semiconductor laser with a symmetric Fano resonance. As shown in Fig. 2-2a, the mean-field behavior can differ drastically depending on the sharpness of the loss $\kappa_n = \partial\kappa/\partial n$.

The mean-field dynamics of the equations of motion allow diverse modes of operation, as shown in Fig. 2-2a. The key driving force for these behaviors is the variation in the damping rate for relaxation oscillations (Eq. 2.5), which describes relaxation back to the mean field steady state. We plot the temporal evolution of the intracavity photon number following a transient 10% increase in the photon number at $t = 0$ relative to the initial steady state. For $\kappa_n \approx 0$ (low n and far detuned from Fano resonance, blue region), relaxation oscillations are observed. For $\kappa_n \ll 0$, the relaxation oscillations become critically damped and eventually undamped (orange region), resulting in oscillations that transition into self-generated and self-sustained pulses. The pulses are quenched when the initial photon number enters the bistable region's lowest branch (demarcated by gray lines in Fig. 2-2b), ultimately collapsing to the topmost branch (and bypassing the intermediate unstable branch). For $\kappa_n > 0$, relaxation oscillations are strongly damped (Γ_1 grows with κ_n in Eq. 2.5). We note that in many semiconductor lasers that are not operated very far above threshold, intensity noise is often far from the shot noise limit due to the relaxation oscillation peak. The nonlinear loss in the region $\kappa_n > 0$ suppresses this peak by over four orders of magnitude, as we will show. Physically, the nonlinear loss magnifies the strength of attraction of the laser steady state (a fixed point of the rate equations) in proportion to the slope κ_n. This has the effect of strongly resisting deviations from the steady state photon number, leading to the strong intensity squeezing described in the next section.

Self-pulsing has been reported previously using photonic crystal-based "Fano" lasers with saturable free carrier absorption from a nanocavity [1]. Here, we see that a similar phenomenon occurs due to a different physical mechanism: the combination of Kerr nonlinearity and dispersive loss. Suppose that the laser is pumped to a CW steady-state lying in the self-pulsing region of Fig. 2-2a. A transient increase in intracavity intensity (e.g., due to spontaneous emission into the lasing mode) now decreases the photonic loss, providing a positive feedback mechanism that builds up the intracavity intensity further. This should continue up to the point where the stimulated emission rate is high enough to drop the carrier density below threshold.

The pump then builds up the carrier density again, and the pulsing continues. Further details about the self-pulsing behavior, including an analysis of the pulse profile, are provided in the Appendix.

We now examine the steady-state input-output curve (S-curve), as shown in Fig. 2-2b. Linear loss presents an n-independent loss profile, and leads to the well known linear dependence of steady state photon number on pump current (as well as clamping of the carrier density and gain above threshold). In the presence of dispersive loss, moderate nonlinearity ($\beta = -10^{-10}$) begins to modify the steady state behavior. For pump currents just above threshold, the behavior is close to linear. However, as the pump current increases, so does the loss, pulling down the input-output curve to a sub-linear behavior. For even stronger nonlinearity ($\beta = -10^{-9}$), a bistable transition occurs that creates a range of photon numbers which have no stable steady state solution. In particular, this occurs because there is a nonzero photon number at which the cavity experiences minimum loss. The topmost bistable branch (with $\kappa_n \gg 0$ and strongest squeezing) needs to be accessed hysteretically "from above," by pumping to a high power (beyond the right bistable edge) and slowly lowering the power.

2.3.2 Broadband intensity noise squeezing

We now describe how the mechanism of intensity-dependent loss can compress steady state photon statistics (Fig. 2-3a). The steady states of all lasers are characterized by a balance between saturable gain and loss. In a conventional laser with "linear loss," the loss rate seen by the cavity field is the same for all photon numbers. For photon numbers where gain exceeds loss, an effective "force" encourages occupation of yet higher photon numbers; for photon numbers where loss dominates gain, an effective force encourages occupation of lower photon numbers. The intersection point where "gain equals loss" represents the equilibrium point between these two forces, and consequently determines the mean photon number of the cavity in the laser steady state. While the intersection point determines the mean photon number, the behavior of the photon number-dependent gain and loss in the vicinity of this

intersection dictates the variance of the photon number probability distribution $p(n)$. In conventional lasers which are far above threshold, the probability distribution approaches that of a coherent state, with Poissonian statistics.

This situation changes significantly when linear loss is replaced by a strongly intensity-dependent loss. If the loss rises sharply with photon number around its intersection with the saturable gain, then the steady state probability distribution becomes compressed compared to the case of linear loss. Intuitively, this is because the disparity between loss and gain around the steady state is magnified relative to the conventional laser, resulting in larger "forces" that squeeze the probability distribution to sub-Poissonian statistics. Roughly speaking, the photon number variance is determined by the ratio of the slopes of the gain and loss. This mechanism enables the sharp loss laser to create steady states with variance lower than the mean, a feature only possible in non-classical light. In the most extreme limit, the loss may rise so sharply that only a single number state (the mean) has a substantial probability of occupation, approaching a cavity Fock state. However, realizing intracavity Fock states would likely require systems with fewer photons and stronger nonlinearities, such as exciton-polariton condensates [33].

To quantify this effect in semiconductor laser systems, we consider the photon number variance, given by $(\Delta n)^2 = \frac{1}{\pi}\int_0^\infty d\omega \langle \delta n^\dagger(\omega)\delta n(\omega)\rangle$, where $\delta n(\omega)$ gives the spectrum of intensity fluctuations and is governed by Eq. 2.4. A useful parameter to quantify the quantum nature of light is the Fano factor, defined as $F = (\Delta n)^2/n$. The Fano factor is 1 for Poissonian light, corresponding to the shot noise limit; values below one indicate sub-Poissonian light below the shot noise level. We calculate the most general expression for F (including carrier nonlinearity) in the presence of nonlinear dispersive loss in the Appendix. For weak Kerr and carrier nonlinearities, $F \to 1$ when pumping far above threshold, approaching Poissonian (coherent) statistics. Our main result here is that for strong Kerr nonlinearity ($n\kappa_n \gg \kappa_0, n|\kappa_N|, \gamma_\parallel, G_N$), the Fano factor behaves as

$$F \to \kappa/(n\kappa_n) \tag{2.6}$$

for large n. Critically, the ratio κ_n/κ is a measure of how sharply the loss varies with n compared to the absolute loss rate at the steady state photon number, and thus dictates the dimensionless "sharpness" of the loss. The Fano factor is inversely proportional to this sharpness factor, and thus sharp losses can lead to sub-Poissonian states.

In Fig. 2-3, we demonstrate the effects of intensity noise squeezing in semiconductor lasers with nonlinear dispersive loss. Just above the left point of bistability, n stays approximately constant while the photon number variance Δn^2 can decrease sharply. In the plot of the Fano factor spectrum $\Delta n^2(\omega)/n$ (Fig. 2-3b), the intensity noise fluctuations associated with relaxation oscillations (ROs) are quenched closer to the left bistable point. Due to the sharp loss, the RO peak is in general significantly suppressed compared to the case of linear loss (the RO frequency and damping rate are increased in accordance with Eq. 2.5). Note that as a result of the bistability, the laser can exist in two states with very different photon numbers over a range of pump currents. The larger photon number branch corresponds to sharp loss ($\kappa_n > 0$) in this scheme. Overall, nonlinear dispersive loss creates significant broadband intensity noise squeezing by orders of magnitude compared to analogous linear loss.

We also found that intensity noise squeezing can extend to the light which exits the cavity. To analyze this effect, the output noise spectrum can be computed from the intracavity noise spectrum by coupled mode theory (see Appendix for details). In Fig. 2-3c, we plot the output intensity spectrum normalized to the shot noise limit (SNL) for three different pump powers (with $\beta = -10^{-9}$). When a shot noise limited pump is used, output photon noise is not squeezed below the SNL. By using "quiet" pumping (i.e. constant current driving), it is possible to achieve noise reduction exceeding 10 dB below the SNL over GHz bandwidths. In conventional semiconductor lasers that are quietly pumped, weak output squeezing has been experimentally observed at sub-GHz bandwidths and strong squeezing (> 10 dB) is only predicted to occur for operation far above threshold and is not associated with intracavity squeezing [39]. In contrast, the mechanism of nonlinear dispersive loss (1) creates strongly squeezed intracavity states, (2) strongly suppresses the relaxation oscillation peak (> 12 dB relative to a

conventional semiconductor laser with the same pump current but without nonlinear dispersive loss), extending output squeezing to GHz bandwidths, and (3) may allow significant output squeezing even at moderate pump currents owing to the bistability that creates strong intracavity squeezing near threshold for nonzero photon number.

Finally, we calculate noise frequency-integrated Fano factors as a function of pump current in Fig. 2-3e by integrating the spectra in Fig. 2-3b. For linear loss, the Fano factor approaches unity (shot noise limit) far above threshold. The behavior of Fano factor for nonlinear dispersive loss is phenomenologically different. For simplicity, in Fig. 2-3e, we only plot the sharp loss (upper) branch when bistability is present (purple curves). We note that the lower branch, accessible by normal pumping from threshold, resembles linear behavior apart from the bistable point, which creates a discontinuity in the Fano factor as a function of pump current. On the upper branch, linear behavior (shot noise) is restored when the detuning from the Fano resonance grows large ($\kappa_n \approx 0$). Approaching the left bistable edge, the cavity frequency approaches the Fano resonance and, for a certain n, the ratio $\kappa/(n\kappa_n)$ approaches a minimum, corresponding to maximum intracavity squeezing. The Fano factor does not decrease indefinitely due to intensity-carrier noise coupling and finite carrier noise from nonradiative decay processes. Nonetheless, low linear background losses, sharp dispersive dissipation, and large Kerr nonlinearities can create intracavity squeezing over 10 dB below the shot noise limit.

We next consider a second kind of dispersive loss – distributed feedback provided by, for example, a distributed Bragg reflector (DBR). This type of loss marks a departure from the adiabaticity criterion that limits the sharpness of Fano-type losses because its timescale is instead set by the width of the DBR pass/stop band, not the sharpness of its decay. In principle, this means that the DBR-type loss can be made quite large, enhancing intensity noise squeezing further. This is shown in Fig. 2-3c,e, where sharper loss profiles (obtained by increasing the number of layers in the DBR) correspond to enhanced squeezing (5 dB lower than the Fano mirror example in Fig. 2-3d). Additionally, the sharp loss region ($\kappa_n > 0$) in the case of DBR loss profiles can be accessed by pumping directly from threshold, where a stop band transitions to

a pass band. Further details about the DBR example, including the exact analytical form for the loss, are provided in the Appendix.

2.3.3 IR and terahertz squeezing using quantum cascade lasers

To emphasize the generality of the physics of nonlinear dissipation, we apply this mechanism to quantum cascade lasers (QCLs), showing that strong intensity squeezing can be extended to "difficult" spectral ranges where squeezing has not been demonstrated, such as the mid-IR and THz. QCLs employ intersubband transitions for stimulated emission, allowing recycling of the carrier population and therefore high output powers, since a single carrier can now generate m photons if m gain stages are used [40, 41]. This endows QCLs with giant intrinsic Kerr nonlinearities that have been employed in a variety of applications, such as frequency comb generation for molecular spectroscopy in the infrared [42]. We note that the picosecond timescale of these nonlinearities can fulfill the adiabaticity criterion for nonlinear dispersive loss [43] and that low-loss dispersive mirrors have been previously used to create dispersion-compensated QCL frequency combs [44]. Strongly intensity noise-squeezed light from QCLs, if realized, is extremely promising given that (1) intensity noise squeezing is more difficult to achieve in QCLs than other semiconductor lasers due to nonradiative decay of carriers in multiple levels [3], and (2) QCLs operate at wavelengths that are of great interest for sensing applications but are inaccessible by most other lasers.

A sample design for a QCL with nonlinear dispersive loss is provided in Fig. 2-4a. Here, the intrinsic Kerr nonlinearity of the active region combined with a dispersive mirror on the laser's output facet generates nonlinear dissipation. To quantify the steady state and noise behavior of this system, we proceed by a Langevin force-based rate equation analysis as before. We use a three-level model for the carrier dynamics (Fig. 2-4b, c), with rate equations describing the evolution of the photon and carrier populations provided in the Appendix. The nonradiative decay time constants governing transitions between the three carrier levels are given by $\tau_{31}, \tau_{32}, \tau_{21}$ and linear gain proportional to the difference in population between levels 2 and 3 is

assumed.

We calculate intracavity intensity noise spectra and integrated Fano factors by Fourier transforming the linearized rate equations (as done above), with details of the calculation provided in the Appendix. We find that the DC/low-frequency noise is suppressed by a factor $(n\kappa_n/\kappa)^2$ in the presence of strong nonlinear loss, $n\kappa_n \gg \kappa, 1/\tau_{21}, 1/\tau_{31}, 1/\tau_{32}$. We plot the noise behavior for a sample system with Fano mirror outcoupling in Fig. 2-4d, e. In this figure, we consider steady state and noise for three different Kerr nonlinear strengths β and two different operating wavelengths λ_0 to mimic realistic experimental systems operating in the IR and THz. For comparison, we note that per-photon nonlinear strengths $\beta \sim 10^{-10}$ were observed nearly two decades ago when QCLs were first used for self-mode-locking [45]. Our results show that the strong, ultrafast Kerr nonlinearity in QCLs in combination with dispersive loss mechanisms can be harnessed to generate strong broadband intensity noise squeezing that has generally evaded mid-IR and THz wavelengths. Note also that (1) QCLs do not suffer from the GHz relaxation oscillations present in conventional semiconductor lasers due to the ultrafast (intersubband) carrier dynamics [46] and (2) linewidth enhancement due to free carriers is negligible, so the cavity resonance frequency $\omega_R(n, N) \rightarrow \omega_R(n)$ and the nonlinear loss $\kappa(n, N) \rightarrow \kappa(n)$. We finally note that self-pulsing by the mechanism in Sec. 2.3.1 in QCLs may be possible but is more difficult to achieve than in conventional diode lasers. This is due to the ultrafast (intersubband) carrier dynamics in QCLs, which create high frequency (exceeding GHz) relaxation oscillations that are difficult to undamp.

2.4 Discussion

We briefly describe some of the other experimental platforms for realizing the effects of nonlinear dispersive loss. We have already shown how quantum cascade lasers (QCLs) are promising realizations of semiconductor lasers with nonlinear dispersive loss given their giant, ultrafast Kerr nonlinearities. QCLs emit at IR and THz wavelengths, overlapping with the vibrational modes of many biochemically relevant molecules,

making the possibility of developing quantum-enhanced chemosensors based on the principles described here tantalizing.

Because semiconductor platforms are conducive to integration with on-chip photonic crystal optical elements, many designs have already achieved the dispersive losses considered here and therefore could exhibit intensity noise reduction if quality factors and nonlinear strengths are within the tolerances required. For example, previous work has realized "Fano lasers" that exhibit self-pulsing due to the interplay between dispersive loss and carrier nonlinearity [1]. A Fano resonance is created by coupling between a waveguide and nanocavity (point defect) in a photonic crystal slab. By increasing the quality factor of the lasing waveguide mode in these types of structures and integrating a Kerr material in/around the gain region, intensity noise reduction by nonlinear dispersive loss could be observable (Fig. 2-1c).

Photonic crystal surface-emitting lasers (PCSELs) are another platform that may be used for demonstrating the effects of nonlinear dispersive loss [47]. PCSELs may present advantages such as single-mode operation and high output powers; in contrast to the Fano laser concept, lasing occurs transversely (and thus the Fano mirror is aligned transversely rather than longitudinally). However, because losses may be significant in both longitudinal and transverse directions, it is necessary to optimize quality factors in both directions. The use of bound states in the continuum is also a promising way forward to achieve high quality factor resonances and nonlinear dissipation when PCSELs are endowed with strong Kerr nonlinearity [48].

In addition to Fano-type dispersive losses, distributed feedback-based losses have been commonly exploited to enforce single-mode operation. Examples include distributed Bragg reflector (DBR) fiber lasers, vertical cavity surface-emitting lasers (VCSELs), and DBR diode lasers [49, 50]. All of these architectures include sharply frequency-dependent elements that may be used to achieve strong noise condensation. High quality fabrication is necessary to minimize background losses (e.g., scattering) at interfaces in order to observe the intensity noise condensation described here.

Furthermore, we note that even stronger nonlinearities may be achievable in systems such as microdisk and quantum dot lasers due to enhanced confinement and

ultralow mode volumes [51]. For mode volumes achieving λ^3, the dimensionless Kerr coefficient can be orders of magnitude larger than the values considered here. Lastly, combining our methodology with recent proposals for nanolasers with strong subwavelength confinement [52] could yield even further intensity noise reduction in output noise.

2.5 Outlook

In this project, we have shown how semiconductor lasers with sharply frequency-dependent outcoupling and Kerr nonlinearity can be used to create lasers which possess intrinsic bistability and self-pulsing capabilities in the classical domain as well as high levels of quantum mechanical intensity noise squeezing both inside and outside the laser cavity. The squeezing occurs across a huge bandwidth in noise frequency, giving rise to near-Fock states with strong squeezing in photon number. Furthermore, we have shown that the squeezing is achievable from IR to THz wavelengths, potentially unlocking numerous applications in sensing, computing, and metrology. We anticipate that many existing experimental platforms could realize the intensity noise reduction, bistability, and self-pulsing effects described here, especially systems employing a geometry that maximizes photonic (Kerr) nonlinearity.

This work naturally suggests additionally possibilities for using nonlinear dispersive dissipation to control the output state of semiconductor lasers. Examples of topics for additional investigation include the effect of nonlinear dispersive loss on phase noise and linewidth, the effects of optical feedback on pulsing, bistability, and intensity/phase noise (e.g., in external cavity lasers), and the simultaneous control of self-pulsing and squeezing to generate pulsed squeezing. Semiconductor lasers are ubiquitous in many real-world applications and we envision that the use of nonlinear dispersive loss could render them novel tools to control the mean field and noise behavior of light across a wide range of wavelengths.

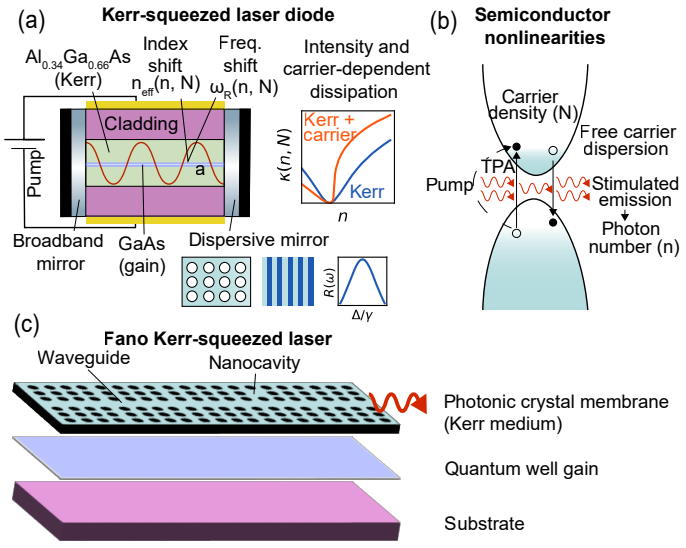

Figure 2-1: **Semiconductor lasers with nonlinear dispersive loss.** (a) Basic semiconductor laser diode heterostructure design with nonlinear dispersive loss. Dispersive outcoupling is generated via the sharp frequency-dependent transmission of a photonic crystal element. Coupling of Kerr nonlinearity from the Kerr material and carrier nonlinearity from the gain material with a dispersive mirror of reflectivity $R(\omega)$ creates sharp nonlinear loss $\kappa(n, N)$. Here, Δ denotes detuning from the dispersive (Lorentzian) resonance and γ denotes the width of the dispersive resonance (related to its FWHM). (b) Semiconductor optical nonlinearities, including carrier-dependent free carrier dispersion (FCD) and two photon absorption (TPA). In addition to the photon number-dependent Kerr effect, these nonlinearities shift the real part of the active region's refractive index, in turn shifting the resonance frequency in the laser cavity. Weak nonlinear loss from shifting the imaginary part of the refractive index via the Kramers-Kronig relations is also generated, but in most cases is negligible compared to the nonlinear dispersive loss. (c) Sample implementation of nonlinear loss in a photonic crystal (PhC) "Fano" laser. The PhC platform allows much stronger per-photon nonlinearities due to very small mode volumes. Dispersive loss is provided by waveguide-nanocavity Fano interference in a photonic crystal slab [1].

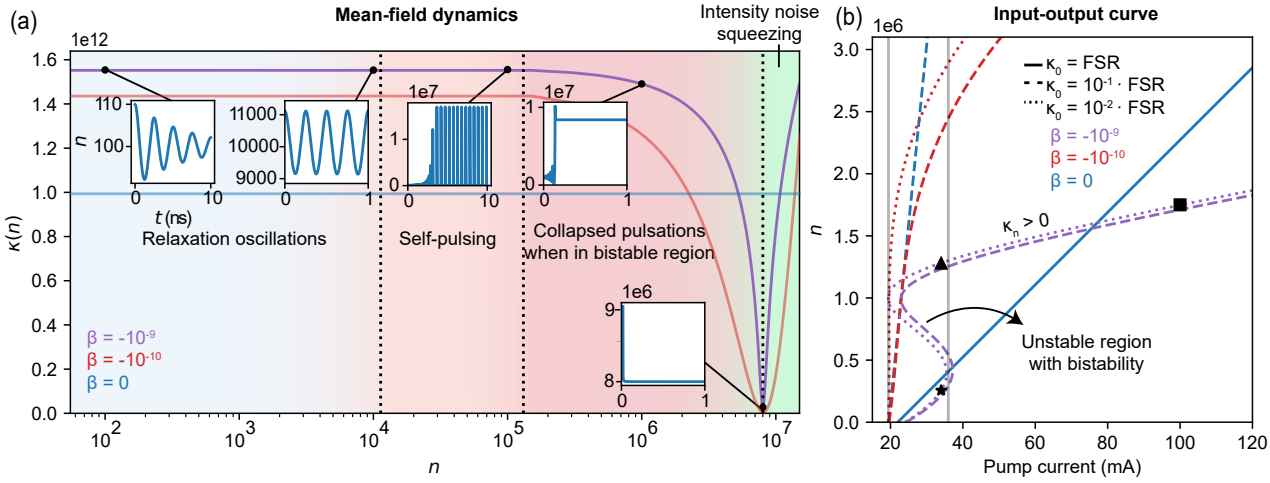

Figure 2-2: **Mean-field dynamics and steady state behavior.** (a) Dynamical and steady state solutions in semiconductor lasers with nonlinear dispersive loss. In the region $\kappa_n = \partial\kappa/\partial n < 0$ (photon numbers left of the Fano resonance), a variety of different behaviors are possible. At large detunings (small n, blue region), the loss does not depend strongly on photon number, and the relaxation oscillations typical of conventional semiconductor lasers are observed. At a certain detuning (n), the relaxation oscillations become critically damped and, at smaller detunings, they become undamped, leading to self-sustained picosecond pulses (orange region). When the pump enters the bistable region (red region, only present for $\beta = -10^{-9}$ (purple curve)), the pulses become transient and the laser ultimately collapses to a continuous wave (CW) steady state. Lastly, to the right of the loss minimum (green), relaxation oscillations are heavily damped since $\kappa_n = \partial\kappa/\partial n > 0$, leaving a CW steady state. Plots were produced by considering a transient increase in intracavity intensity by 10% at $t = 0$ relative to steady state. (b) Steady state intracavity photon number n as a function of pump current (S-curve) for three different linear background losses κ_0 and nonlinear strengths β. The indicated unstable region is bypassed by the bistable point and is not generally accessible during lasing. The gray vertical lines denote the boundaries of the bistable region for the purple dotted curve. In these simulations, we use parameters based on experimentally determined values for buried heterostructure lasers with GaAs gain and AlGaAs cladding (Fig. 2-1a): active region dimensions 0.1 μm × 5 μm × 1 mm, confinement factor $\Gamma = 0.3$, bare cavity resonance frequency $\omega_0 = 2.16 \times 10^{15}$ s^{-1} (873 nm, GaAs bandgap), free spectral range FSR = 43 GHz, transparency density $N_{\text{trans}} = 2 \times 10^{24}$ m^{-3}, nonradiative decay rate $\gamma_{\parallel} = 3 \times 10^{8}$ s^{-1}, and linear gain coefficient $G_N = 1/V \cdot dG/dN = 3694$ s^{-1} [2]. The Appendix provides an estimate of typical Kerr nonlinear strengths in this structure. The Fano resonance is centered at photon number $n_c = 8 \times 10^6$ (a) and $n_c = 10^6$ (b). Its resonance decay (FWHM) is $\gamma = 2 \times 10^{12}$ s^{-1}. In (a), $\kappa_0 = 10^{-2} \cdot \text{FSR}$ for $\beta \neq 0$.

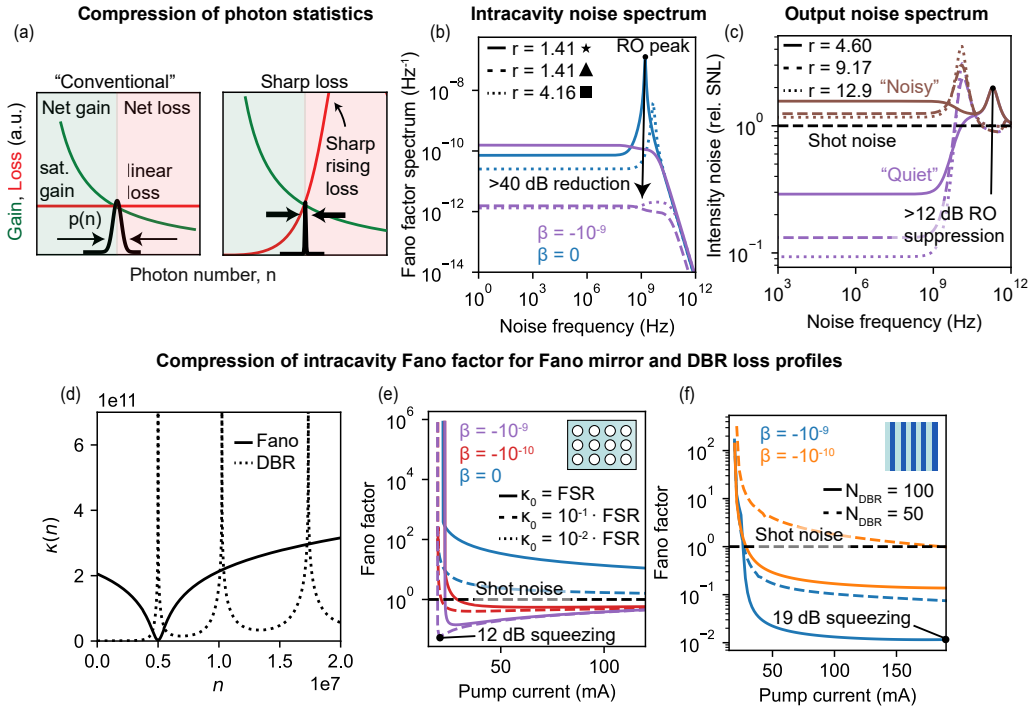

Figure 2-3: **Intensity noise squeezing.** (a) Comparison of steady state photon probability distribution $p(n)$ under conventional and sharp loss. The steady state photon number is determined by the location of intersection between saturable gain and loss. The variance of the probability distribution is determined by the effective "steepness" of intersection of the gain and loss curves. While the conventional laser architecture with linear loss results in a near-coherent state far above threshold, the sharp loss architecture results in states with variance below the mean, which correspond to non-classical light. In the most extreme limit, this mechanism can enable the generation of near-Fock states inside the laser cavity. (b) Intracavity Fano factor spectrum ($\Delta n^2(\omega)/n$) as a function of noise frequency for the three different steady states (★, ▲, ■) indicated in the input-output curve of Fig. 2-2b ($r \equiv I/I_{\text{thres}}$ is the pumping ratio). Here, $\kappa_0 = \text{FSR}$ for the linear loss (blue) and $\kappa_0 = 10^{-2} \cdot \text{FSR}$ for the nonlinear loss (purple). Nonlinear loss creates a strong suppression of the relaxation oscillation (RO) peak. (c) Output squeezing over a > 1 GHz bandwidth with ("noisy") and without ("quiet") pump noise suppression (plotted for three different pump powers with nonlinear strength $\beta = -10^{-9}$). (d), (e), (f) Comparison of loss profiles and integrated Fano factor as a function of pump current for a nonlinear laser with a Fano mirror or DBR. Fano factors are plotted for the low noise branch when bistability is present. In (d), (e), (f), $n_c = 5 \times 10^6$ marks the center of the Fano resonance, while for DBR loss profiles, the average index is $\tilde{n} = 3.0$, the index contrast is $\Delta n \lesssim 1.0$, and the first transition from stop to pass band is tuned to occur around $n_c = 5 \times 10^6$. All other simulation parameters are the same as those in Fig. 2-2.

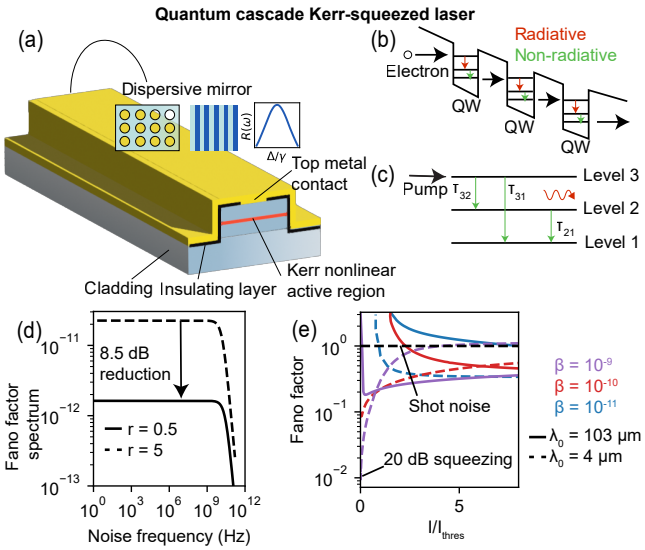

Figure 2-4: **Strongly squeezed IR and terahertz light using QCLs.** (a), (b) Basic dispersive Kerr-squeezed QCL laser architecture with nonlinear dispersive loss. Electrons make subband transitions in a given quantum well and tunnel to the next one. Dispersive outcoupling is provided by a photonic crystal fabricated on an end facet of the QCL. The giant, ultrafast Kerr nonlinearity of the active region due to intersubband transitions is used to generate nonlinear dispersive loss. (c) Three-level system used for rate equation analysis with nonradiative decay timescales from each level indicated. (d) Fano factor spectrum for two different pump strengths $r \equiv I/I_{\text{thres}}$, with $\beta = 10^{-9}$ and $\kappa_0 = \text{FSR}$. A similar bistability to the diode laser case is present here, and the $r = 0.5$ curve is for the upper (low noise) branch ($r = 5$ corresponds to large detuning from the Fano resonance and lies in the approximately linear loss regime). (e) Integrated Fano factor as a function of pump strength for the low noise branch for three different nonlinear strengths and operating wavelengths in the IR and THz. For these simulations, we use system parameters measured from experiment: wavelength $\lambda_0 = 4,103$ μm (IR, THz), $\tau_{32} = 2.1$ ps, $\tau_{31} = 3.4$ ps, $\tau_{21} = 0.5$ ps, $m = 25$ gain stages, confinement factor $\Gamma = 0.2$, cavity length $L = 3$ mm, and gain coefficient $G_N = 10^5\Gamma$ s^{-1} [3, 4]. The Fano resonance has FWHM $\gamma = 2 \times 10^{12}$ rad/s and is centered at $n_c = 2.5 \times 10^7$.

Chapter 3

Multimode squeezing and quantum correlations using cascaded nonlinear optical processes

The content of this chapter is taken largely from my first author preprint [53].

3.1 Introduction

Quantum states of light prepared using nonlinear parametric processes have attracted significant interest for applications in precision measurement and quantum technologies through noise squeezing and entanglement properties [8, 54–56]. Second order nonlinear processes have emerged as a key platform to generate quantum states of light by processes including second harmonic generation and parametric downconversion in optical parametric oscillators (OPOs), leading to numerous theoretical proposals and experimental realizations of entangled single photon pairs, single mode squeezing, squeezed supermodes (including two-mode squeezing), and broadband quantum frequency combs [12, 13, 57–67]. However, most of these works have focused on single mode and multimode squeezed vacua (as generated, for example, by OPOs pumped below threshold). Nondegenerate OPOs operated above threshold have also been investigated for amplitude squeezing. In many works, twin beam squeezing is often

considered, given the strong correlation between intensity noise in signal and idler modes from a single parametric downconversion process. Single beam squeezing is also possible, considering the photon number filtering that twin beam correlations induce [68–70]. However, the output amplitude noise squeezing for a single nondegenerate downconversion process is theoretically limited to 3 dB below the shot noise limit [68]. This squeezing is also generally limited to narrow spectral ranges depending on the nonlinear crystal used and its phase matching conditions. Achieving tunable single mode and multimode "bright" amplitude squeezing in systems with multiple frequency modes remains unexplored, despite exciting potential for quantum optical information multiplexing and bright squeezed frequency combs for spectroscopy applications [71].

Here, we explore a novel scheme for amplitude squeezing within a multimode cavity with second-order nonlinearity that employs cascaded parametric amplification mediated by a common terahertz "bath" mode to create an infrared frequency comb with terahertz mode spacing [72–74]. We demonstrate that by strategically engineering the cavity's Q factor profile, we can manipulate the nonlinear energy flow through frequency space, thereby significantly shaping both mean field and noise properties. Our method works by creating a high Q factor cavity in frequency space that traps nonlinear energy flow within a finite (and controllable) span of discrete frequency modes [75]. This enables very strong nonlinear coupling between nearest-neighbor frequency modes that can exceed decay rates in the system. This can lead to excitation of counter-propagating Bloch modes in the "frequency cavity," whose interference is manifested in a standing wave distribution of steady state modal energies. By increasing the outcoupling (lowering the loaded Q factor) for one or more selected discrete frequency modes, we show that the frequency cavity supports simultaneous output amplitude squeezing in these mode(s) over a > 100 MHz bandwidth. Strong squeezing emerges because of an enhancement in the noiseless nonlinear coupling over dissipation. Finally, we describe how the strong nonlinear interactions in our system create strong long-range correlations in amplitude noise that may suggest existence of long-range entanglement in a synthetic frequency dimension. Our study of quantum

noise through cascaded nonlinear interactions suggests many exciting possibilities, including bright squeezed frequency combs, trapped states and solitons in the synthetic frequency dimension, tunable quantum walks, and much more [75].

The rest of this chapter is structured as follows. In Sec. 3.2, we introduce our system and describe how its mean field dynamics and quantum noise behavior can be calculated. Included in this section is a discussion of the "frequency cavity" that our system realizes, which supports counter-propagating resonant Bloch modes that cause interference patterns in the modal energy distribution. In Sec. 3.3.1, we describe intracavity mean field dynamics, noise, and the presence of relaxation oscillations due to strong multimode nonlinear coupling. In Sec. A.4, we show tunable single mode and multimode squeezing in output amplitude noise, describing the limitations and conditions for generating strong squeezing. Lastly, in Sec. 3.5, we show how the coupling of the infrared frequency comb to a common terahertz bath mode allows strong long-range correlations in frequency space.

3.2 Theory

At the heart of our concept is the novel Q engineering of a multimode nonlinear cavity [76], as illustrated in Fig. 3-1a. Our system comprises a comb of infrared (IR) cavity modes, each mode coupled to its nearest neighbors via a bath mode, here specifically a terahertz (THz) frequency mode (whose small frequency allows for many modes in a small IR span). The process begins with nonlinear three wave mixing (TWM) where a pump photon (ω_0) simultaneously amplifies a seed photon (ω_1) and generates a new photon in the idler "bath" mode (ω_T). Subsequently, cascading steps are initiated by the nonlinear interaction of the bath mode (THz) with the IR modes, resulting in multiple equally spaced modes. This produces a frequency comb with spacing given by ω_T. By properly engineering the Q factors of the cavity modes, one can favor the three wave downconversion processes that create THz idler photons. This enhances the rate of nonlinear energy flow in the cavity and, due to its noiseless nature, can result in squeezing when the nonlinear rate surpasses dissipation rates in

the system.

We design the multimode cavity such that, through phase matching constraints, only TWMs of the form $\omega_{n-1} \leftrightarrow \omega_n + \omega_T$ are supported (here, $\omega_k < \omega_n$ when $k > n$). The decay rates for modes of all other frequencies are assumed much faster than the relevant timescales in this system, so we restrict our attention to the system specified by the coupled IR modes and the THz mode.

We simulate the mean field and noise properties of our system by using the Heisenberg-Langevin equations of motion for the mode field (annihilation) operators (see Appendix for details), which read

$$\begin{aligned} \dot{a}_T &= \kappa \sum_n a_n^\dagger a_{n-1} - \gamma_T a_T + \sqrt{2\gamma_T} s_T \\ \dot{a}_n &= \kappa \left(a_T^\dagger a_{n-1} - a_{n+1} a_T \right) - \gamma_n a_n + \sqrt{2\gamma_n} s_n, \end{aligned} \tag{3.1}$$

where a_n are field operators that determine the photon number $\langle a_n^\dagger a_n \rangle$, $\kappa \in \mathbb{R}$ has units of s^{-1} and denotes the nonlinear coupling strength (related to the nonlinear susceptibility $\chi^{(2)}$ and assumed frequency-independent), γ_n, γ_T denote the outcoupling rates for the IR and THz modes, s_n denotes the external fields, and the indexing is such that $n > 0$ correspond to redshifted modes relative to the pump at $n = 0$. An estimation of typical values of κ for realistic experimental settings is provided in the Appendix. Unless specified otherwise, only modes $a_{0,1}$ are pumped, so that only $s_{0,1}$ have nonzero mean. Note that in the Heisenberg-Langevin formalism, the zero-mean terms $\sqrt{2\gamma_n} s_n$ are Langevin forces associated with the outcoupling process (see Appendix). In Sec. A.4, we consider the effect of intrinsic loss, which adds further noise to the system through other Langevin forces (the full equations of motion including intrinsic loss are provided in the Appendix). In our simulations, we numerically solve the Heisenberg-Langevin equations of motion in the mean field domain using backward differentiation [1] to obtain the steady state mode amplitudes $a_n \equiv \langle a_n \rangle, a_n^* = \langle a_n^\dagger \rangle$ from a vacuum initial state.

Assuming a strong, coherent pump (up to small fluctuations), when the system

[1] This allows us to handle numerically stiff systems with strong nonlinearity.

reaches steady state, we can linearize the equations of motion about the mean values for the fields ($\hat{a}_n = a_n + \delta\hat{a}_n$ where here we made explicit the distinction between an operator and complex number) to construct linearized equations of motion for the operators $\delta a_n, \delta a_n^\dagger$. Note that we do in general need to linearize with respect to two degrees of freedom for each mode $(a_n, a_n^\dagger)$. However, by picking zero initial conditions for the fields and taking $\kappa \in \mathbb{R}$, the steady states will be real-valued in this model. Then, we can define quadrature operators $p_n = a_n + a_n^\dagger, q_n = -i\left(a_n - a_n^\dagger\right)$, whose fluctuations directly give the amplitude and phase noise of mode a_n (as shown in the Appendix). Because the modal amplitudes are real-valued, p_n, q_n do not couple. We can perform a Fourier transform and derive a system linear in the fluctuations $\delta p_n(\omega)$ that can be arranged in matrix form as $M(\omega)P(\omega) = F(\omega)$, where $P(\omega) = [\delta p_0(\omega)\delta p_1(\omega)\cdots\delta p_N(\omega)\delta p_T(\omega)]^T$ and $F = [F_0(\omega)F_1(\omega)\cdots F_N(\omega)F_T(\omega)]^T$ is the Langevin force vector. The zero-mean Langevin forces satisfy $\langle F_n^\dagger F_{n'}\rangle = 2\gamma_n\delta_{nn'}$ (see Appendix for details). An explicit expression for the fluctuation matrix M is also provided in the Appendix. The amplitude noise for mode a_n is coupled to the noise of a_T, a_{n-1}, a_{n+1} in the frequency domain according to

$$\delta p_n = \frac{\kappa\left[\delta p_T(a_{n-1} - a_{n+1}) + a_T(\delta p_{n-1} - \delta p_{n+1})\right] + F_n}{-i\omega + \gamma_n}. \tag{3.2}$$

From the elements of the inverse fluctuation matrix M^{-1} as well as the Langevin force correlators, the intracavity and output amplitude noise can be computed according to

$$\begin{aligned}\langle \delta p_{n,\text{in}}^\dagger \delta p_{n,\text{in}}\rangle &= |M_{n,N+1}^{-1}|^2(2\gamma_T) + \sum_{k=0}^{N}|M_{n,k}^{-1}|^2(2\gamma_k)\\ \langle \delta p_{n,\text{out}}^\dagger \delta p_{n,\text{out}}\rangle &= 1 + 2\gamma_n\langle \delta p_{n,\text{in}}^\dagger \delta p_{n,\text{in}}\rangle - 4\gamma_n\text{Re}(M_{n,n}^{-1}),\end{aligned} \tag{3.3}$$

where the output fluctuation amplitude for mode a_n is given by $\delta p_{n,\text{out}} = \sqrt{2\gamma_n}\delta p_{n,\text{in}} - (\delta s_n + \delta s_n^\dagger)$. To compute the squeezing factor, we compare the amplitude noise to the corresponding shot noise limit (SNL) in the absence of any nonlinear processes. Under only driven-dissipative dynamics (and neglecting intrinsic loss), one can show

(see Appendix) that $\langle \delta p^{\dagger}_{n,\mathrm{in}}(\omega)\delta p_{n,\mathrm{in}}(\omega)\rangle = 2\gamma_n/(\gamma_n^2+\omega^2)$ and $\langle \delta p^{\dagger}_{n,\mathrm{out}}(\omega)\delta p_{n,\mathrm{out}}(\omega)\rangle = 1$. These represent what we will use as "reference coherent states" when analyzing intracavity and output noise in our system. As we will show, enhancement of nonlinear coupling can enable destructive interference between the vacuum field s_n and the intracavity field $p_{n,\mathrm{in}}$, generating output squeezing as shown in Fig. 3-1b.

3.3 Intracavity mean field dynamics and noise

3.3.1 Frequency space cavity

Our system is analogous to the implementation of coupled resonator optical waveguides in a synthetic frequency dimension [77]. When the system is truncated by boundary modes in the frequency dimension, it can be thought of as a Fabry-Perot-type cavity in frequency space defined by the finite extent of the high Q factor cascading orders and bounded by lower Q factor frequency "mirrors." The leakiest modes lie outside the frequency cavity. In Fig. 3-1c, this is shown for a one-sided comb where frequency cavity modes $\omega_{1,\ldots,N-1}$ have high Q factor (Q_r) and frequency mirrors at $\omega_{0,N}$ have lower Q factor ($Q_{0,N}$). A natural consequence is that the excitation of modes in this frequency space cavity should manifest in the steady state energy distribution of the frequency modes. We can make this rigorous by considering a Bloch mode analysis, noting that our system is a kind of nonlinear tight-binding model with quasi-discrete translational symmetry (up to boundary conditions at the frequency mirrors) in the synthetic frequency dimension. As a crude approximation, in the case of linear coupling (i.e. assuming a_T is constant) and neglecting dispersion, we have the result that two counter-propagating Bloch waves with wave vectors $k_{\pm} = \pi/2a$ (where $a = \omega_T$ is the lattice constant of the frequency crystal defined by the cascading frequency modes) are excited [75]. (Though beyond the scope of our work, we note that higher order Bloch modes may be excited by using a pump detuned from ω_0. This provides an extra degree of freedom that could allow synthesis of arbitrary states/modal profiles in the frequency dimension.) Interference of the

Bloch modes creates a modal energy distribution with quasi-periodicity $2a$ (due to dissipation, modal energy drops further from the pump mode). The magnitude of interference can be tuned via the reflectivity of the frequency mirrors. For example, one can minimize interference by creating an open boundary condition at ω_N. This can be done by "impedance matching" mode a_N such that $\gamma_N \approx \kappa a_T$. This results in minimum reflectivity at ω_N. While minimizing interference is advantageous for maximizing efficiency of populating the terahertz idler mode [76], other design methods, which we describe below, are more optimal for maximizing output squeezing.

We briefly note that the interference state in steady state modal energy naturally translates into interference in the low frequency modal amplitude noise from the linearization procedure. In steady state, $a_n \propto a_{n-1} - a_{n+1}$ and at zero noise frequency, $\delta p_n(0) \propto \delta p_T(0)(a_{n-1} - a_{n+1})$ (the first term in Eq. 3.2 is usually dominant since the terahertz mode contains additive noise from all of the TWM processes). Thus, generally, cascading IR modes with higher intracavity intensity are accompanied with higher low-frequency intracavity amplitude noise.

In Fig. 3-2a, b, we show how a Q engineered multimode cavity that favors frequency downconversions enables strong nonlinear energy flow that creates a frequency comb in modes redshifted relative to the pump mode a_0. Fig. 3-2a shows the temporal dynamics of the modal energy distribution for a multimode cavity with Q factor spectrum given by the first panel of Fig. 3-2b. Intuitively, energy "bounces" back and forth between the two frequency mirrors, eventually creating a steady state modal energy distribution that shows Bloch mode interference (excitation of Bloch modes with wavevectors $k_\pm = \pi/2\omega_T$) for the infrared modes lying inside the cavity, as shown in the second panel of Fig. 3-2b. Only modes trapped within the frequency cavity defined by the frequency mirrors at $\omega_{0,N}$ are appreciably occupied. Of additional note is the high energy of the terahertz idler mode in the steady state, reflecting the ability of our system to generate the terahertz idler mode with high efficiency [76]. In the Appendix, we show how one-sided (blueshifted) and two-shifted frequency combs can also be produced in our system with appropriate Q factor shaping.

3.3.2 Intracavity noise

Using the formalism described in Sec. 3.2, we can compute the Fano factor noise spectrum for an arbitrary mode a_n as $\langle \delta n_n^\dagger(\omega)\delta n_n(\omega)\rangle/n_n = \langle \delta p_n^\dagger(\omega)\delta p_n(\omega)\rangle$ (where $n_n = a_n^\dagger a_n, \delta n_n = a_n\delta a_n^\dagger + a_n^*\delta a_n$ denote the intracavity photon number and its fluctuations for mode a_n). In Fig. 3-2c, this noise spectrum is plotted for several frequency modes. The low Q blueshifted modes do not have strong nonlinear coupling with other modes in the system and are governed by driven-dissipative dynamics, generating an intracavity coherent state (blue curve). By contrast, the idler mode (green), cascading infrared orders (red), and pump mode (black) undergo strong nonlinear interactions that dominate their dynamics. This results in strong gigahertz relaxation oscillations (on the order of the characteristic nonlinear rate $|\kappa a_T|$). Several relaxation oscillation peaks are present due to the strong nonlinear coupling between multiple modes within the cavity.

In Eq. 3.3, at frequencies much smaller than the cavity bandwidth, the inverse fluctuation matrix has entries (for the cascading IR orders) governed by the smallest timescale in the system, in our case $M_{n,k}^{-1} \sim 1/\max(\kappa a_T, \gamma_0)$, and the noise for these modes is dominated by the leakiest (lowest Q) mode, which is generally the pump mode a_0. Thus, the low frequency noise for the cascading orders scales as $\langle \delta p_n^\dagger(0)\delta p_n(0)\rangle \sim \mathcal{O}(\gamma_0/\max(\kappa a_T, \gamma_0)^2)$. In Fig. 3-2d, we show how, when compared to the noise of a "reference coherent state" with equivalent loss but no nonlinear coupling, the low frequency noise is of order $\frac{\gamma_0\gamma_n}{\max(\kappa a_T,\gamma_0)^2} \ll 1$ times that of the coherent state. Thus, the intracavity low-frequency noise reduction relative to the aforementioned coherent state is enhanced by maximizing the nonlinear rate κa_T while making the Q factor for all cascading modes large, so that $\gamma_n^2|M_{n,k}^{-1}|^2 \ll 1$. This low-frequency noise reduction can be interpreted as the enhancement of noiseless nonlinear processes relative to dissipative outcoupling which, as we will see, permits output amplitude noise squeezing.

Finally, we note that in the systems we have examined, integrated intracavity noise appears to remain at the shot noise limit due to high frequency relaxation oscillations

(ROs), resulting in multimode intracavity coherent states. System configurations that damp ROs for some (or all) modes and thus permit intracavity squeezing may exist, such as systems with saturable absorbers or other nonlinear losses [5, 78]. Nonlinear dissipation has been proposed as a method to generate strong single mode intracavity squeezing, and its multimode extension should be investigated.

3.4 Output noise squeezing

3.4.1 Single mode squeezing

We now describe how strong output amplitude noise squeezing can be generated using cascaded nonlinear interactions in a multimode cavity. Notice from Eq. 3.3 that there should be strong destructive interference between the intracavity fluctuations of mode a_n and far-field vacuum fluctuations s_n for the same mode (Fig. 3-1b). At the same time, the noise contributions from all other modes should be minimized. Specifically, the conditions to maximize output squeezing read

$$\begin{aligned} &(1) \quad [1 - 2\gamma_n \mathrm{Re}(M^{-1}_{n,n}(\omega))]^2 \ll 1 \\ &(2) \quad 4\gamma_n\gamma_k |(M^{-1}_{n,k}(\omega))|^2 \ll 1, k \neq n, \end{aligned}$$

where $M^{-1}_{n,k}$ is an element of the inverse fluctuation matrix that denotes the contribution of fluctuations in mode a_k to the (intracavity) amplitude noise of mode a_n and γ_n denotes the outcoupling rate for mode a_n. These conditions are satisfied when the mode to be squeezed has a decay rate γ_n on the order of the nonlinear rate κa_T, while the other modes with non-negligible steady-state amplitude are of higher Q factor (and other modes with low Q factor are negligibly occupied). To see this, notice that for an ideal driven-dissipative state at zero noise frequency, $\mathrm{Re}(M^{-1}_{n,n}(0)) = 1/\gamma_n$ so the self-induced noise from condition (1) is at the shot noise limit, while for $\mathrm{Re}(M^{-1}_{n,n}(0)) = 1/(2\gamma_n)$ perfect destructive interference in condition (1) is achieved (zero self-induced noise in the output). In our system, this can be tuned by the ratio $\gamma_n/\kappa a_T$. When all other modes in the frequency comb have high

Q factor, the additive effect on noise in the outcoupled field due to other modes is minimal (condition 2), and squeezing can be observed.

Conditions 1 and 2 determine which discrete frequency modes can be squeezed. It is not possible for the high Q intermediate cascading orders to be squeezed since condition 1 is violated. The external cavity noise for these modes is dominated by external vacuum shot noise. However, mode a_N, for example, terminates the frequency comb and thus has a larger outcoupling (and lower loaded Q factor). When $\gamma_N = \mathcal{O}(\kappa a_T)$, destructive interference of the intracavity amplitude fluctuations with the external vacuum shot noise can occur. Condition 1 can be satisfied through optimizing $M^{-1}_{N,N}$, which in turn can be controlled by the Q factor profile of the cavity. When all other cascading orders (including the pump and seed) are of higher Q factor, both conditions 1 and 2 can be satisfied, yielding strong output amplitude noise squeezing for a_N that exceeds 10 dB over nearly gigahertz bandwidths, as described below.

In Fig. 3-3a, we consider a one-sided comb with $N = 15$ cascading orders where we selectively squeeze a terminal mode ($\lambda_{15} = 1127$ nm) or a mode lying inside the frequency cavity ($\lambda_9 = 1101$ nm) by creating a low Q factor defect for the squeezed mode in the otherwise high Q factor frequency cavity (left panel of Fig. 3-3a). In the center panel, notice that (1) the nonzero reflectivity of frequency mirror a_N generates Bloch interference in the mean field and (2) the low Q factor for the squeezed mode guarantees its large outcoupled power. Satisfying condition 1 (due to the low Q factor of the squeezed mode) and condition 2 (due to the high Q factor of all other coupled modes) generates strong single mode squeezing in low frequency output amplitude noise over 10 dB below the shot noise limit, as seen in the right panel.

In Fig. 3-3b (first panel), we show the contribution of conditions (1) and (2) to the output noise in the terminal mode a_N. The total output noise is minimized when the sum of the two contributions is minimized. We also show the contribution of intrinsic loss to output squeezing (second panel), which reveals that strong squeezing in a_N persists even when intrinsic loss is around 10% of the outcoupling rate, i.e. $\gamma_n/\mu_n \approx 10$ (the same ratio of intrinsic loss to outcoupling is used for all modes).

In Fig. 3-3c, we examine how various setup parameters shape single mode squeezing in the terminal mode a_N. In the first panel, we see that stronger squeezing is achieved for higher Q_T. In addition to enhancing cycling of the terahertz idler photon within the cavity (which strengthens nonlinear energy flow), a higher Q_T reduces the effect of coupling of fluctuations in a_T to output noise in a_N. As expected from condition (1), with fixed Q_T, we see there is an optimal Q_N to generate strongest squeezing. When Q_N is too low or too high, destructive interference with the external vacuum field is ineffective. In the second panel, we sweep over Q_N and the number of cascading orders N. The most distinctive feature is the weakened squeezing for even N. This occurs due to the effect of Bloch interference, specifically the pump mode. When N is odd, the low Q factor end of the frequency space chain a_0, a_{-1} are negligibly occupied, so the squeezing for a_N is strong. When N is even, the noise contribution from a_0, a_{-1} is significant since they are non-negligibly occupied, so the squeezing in a_N is less due to noise coupling to a_0, a_{-1}. We also notice a tendency towards stronger squeezing for longer combs (larger N). This appears to be because of an inverse scaling with N of the coupling of the idler mode fluctuations to the output noise in a_N, due to an enhancement in the effective nonlinear rate relative to dissipation rates. We have found that when condition (1) is fully satisfied, the output noise (relative to the SNL) in a_N goes as $\frac{\gamma_T|a_T|^2}{N^2\gamma_N|a_N|^2}$. This holds as long as the idler mode is the dominant source of (coupled) noise and may break down for very large N when the additive contribution of the noise coupling from the high Q infrared cascading orders becomes significant.

3.4.2 Multimode squeezing

By introducing multiple low Q factor "defects" into the chain of cascading orders, multiple frequency modes can be squeezed in output amplitude noise. When Bloch interference is present, modes with opposite parity to mode a_N have significantly damped low-frequency intracavity noise, so the destructive interference with external vacuum shot noise is ineffective. Therefore, modes $a_N, a_{N-2}, ...$ with the same parity as a_N (high steady-state amplitude, high intracavity noise branch) are more strongly

squeezed. As the number of modes we would like to squeeze increases, the degree of squeezing decreases. Suppose we aim to squeeze m modes by introducing m identical "defects" (Q factor dips). In the ideal case, the noise is dominated by these low Q modes. Let x denote the quantity $2\gamma_n M^{-1}_{n,n}$ for one such squeezed mode. Then, for equal squeezing in all modes, we compute

$$\min_x \left[(1-x)^2 + (m-1)x^2\right] = 1 - \frac{1}{m}. \tag{3.4}$$

Notice that this gives the 3 dB single beam output squeezing limit of the signal and idler beams when $m = 2$ [68]. As m grows large, all modes approach the shot noise limit.

In Fig. 3-3d, e, we show how introducing 1 (a_N squeezed), 2 (a_N, a_{N-2} squeezed), and 3 (a_N, a_{N-2}, a_{N-4} squeezed) defects generates single and multimode output amplitude noise squeezing. By further tuning the Q factors of the squeezed modes, it may be possible to control the "distribution of squeezing" over the squeezed modes (e.g., in the trivial case, only one low Q factor defect corresponds to single mode squeezing). As expected from the previous discussion, the squeezing for multiple modes weakens. The inset shows that the bandwidth over which squeezing occurs is similar to that for intracavity squeezing and limited by the onset of relaxation oscillations. The amplitude noise returns to shot noise level around 100 MHz-1 GHz. This bandwidth is limited by the onset of intracavity relaxation oscillations (i.e. the nonlinear rate in our system). Thus, strong nonlinear interactions can in principle reach GHz-surpassing bandwidths.

3.5 Multimode twin beam quantum correlations

In this section, we examine quantum noise correlations between discrete frequency modes in our system. In the case of a single ideal TWM process, it is well known that the amplitude sum of the signal and idler is noiseless and signal and idler photons are entangled [79]. When cascaded nonlinear processes are present, this entanglement

is now distributed over many modes. In Fig. 3-4, we consider a two-sided comb (in contrast to the one-sided comb design for squeezing above; see Appendix for Q factor profile) and plot the low frequency noise in the output intensity sum $S_{ij} = \sum_{k,k' \in \{i,j\}} \langle \delta n_k^\dagger \delta n_{k'} \rangle$ and difference $D_{ij} = \sum_{k,k' \in \{i,j\}} (-1)^{1+\delta_{k,k'}} \langle \delta n_k^\dagger \delta n_{k'} \rangle$, where $n_k = a_k^\dagger a_k$ is the number operator for mode k (further details on the calculation are provided in the Appendix). These twin beam noises are normalized to the uncorrelated twin beam noise $U_{ij} = \sum_{k \in \{i,j\}} \langle \delta n_k^\dagger \delta n_k \rangle$. Normalization by U_{ij} shows that twin beam squeezing emerges due to *correlations* between the two modes rather than single beam squeezing.

We can compare the twin beam noise to the noise in a single mode. In Fig. 3-4a, we plot the outcoupled power and low frequency output amplitude noise for individual modes. Certain modes are near the SNL, while others are strongly anti-squeezed. Fig. 3-4b demonstrates that twin beam noise can be reduced by orders of magnitude relative to single beam noise. This strong squeezing relative to single beam noise generally occurs when the two modes have comparable individual noise, as this permits stronger destructive interference in the amplitude fluctuations. We see that strong correlations can occur within the frequency cavity and with the common terahertz idler mode, resulting in squeezing over 20 dB relative to the uncorrelated twin beam noise. In contrast to the correlations for a single TWM process, the correlations in our system can be much longer range, spanning the dimension of the frequency cavity. We also point out the twin beam squeezing in the noise of the amplitude difference $p_n - p_{-n}$. This is reminiscent of the strong squeezing reported in the supermodes of soliton microcombs, $p_n \pm p_{-n}$ [64]. We conclude by noting that recent experiments have reported strong noise correlations for multiple wavelength pairs in the continuous spectrum generated by a nonlinear fiber, providing impetus for realizing multimode quantum states over discrete frequency modes [80].

3.6 Discussion

In this project, we demonstrated bright single- and multimode squeezing using cascaded three wave mixing processes in a nonlinear cavity. Our work constitutes a distinct paradigm shift relative to most previous works that have focused on below-threshold parametric squeezing in the single- and multimode regimes. Furthermore, we have shown the existence of quantum correlations between multiple pairs of frequency modes, extending the concept of twin beam squeezing that is well-known for single parametric downconversion processes. In this section, we provide an outlook on this work from both a theoretical and experimental perspective.

We have noted previously that intracavity squeezed state generation in the proposed system is difficult given the existence of high frequency relaxation oscillations. However, the generation of multimode intracavity bright squeezed states could enable a new regime of cavity QED experiments [81–84]. For example, single mode cavity QED is generally limited to global interactions well-described by mean field theory, whereas multimode cavity QED may permit tunable local couplings that can elucidate beyond-mean-field physics [85]. Thus, mechanisms for the suppression of relaxation oscillations should be investigated, such as recent theoretical work on the application of nonlinear dissipation to single mode intracavity squeezing in lasers [5, 78].

Exciting topological phenomena have been studied in synthetic dimensions in photonics, and our work suggests a platform for studying the intersection of topology and nonlinear quantum optics in a synthetic frequency dimension [86, 87]. For example, recent work has explored the use of external amplitude and phase modulation in ring resonators and coupled OPOs to generate non-Hermitian tight-binding coupling between resonant frequency modes [88–90]. Our system offers the opportunity to tune both nonlinear coupling (as we have done here) and non-Hermitian modulation, shaping energy propagation between discrete frequency modes. This could unlock novel topological phenomena such as skin effects in a synthetic frequency dimension and topologically-protected quantum optical states.

Recent work with electro-optic modulated thin-film lithium niobate microres-

onators has revealed the potential of using interference between Bloch modes to tailor the flow of light in the synthetic frequency dimension, creating, for example, trapped states [75]. Applying similar techniques to our system could allow creation of squeezed frequency-space solitons and other more exotic classical and quantum states of light. Additionally, we anticipate that squeezing in these Bloch modes or quasi-Bloch modes that diagonalize the nonlinear Hamiltonian could be even larger than the squeezing for individual frequency modes described here, inspired by recent proposals to generate output squeezing exceeding 15 dB in supermodes of a soliton microcomb system [64].

We now comment on experimental platforms that may realize the effects described here. The important criterion to generate squeezing and strong long-range correlations is a strong enhancement of the nonlinear coupling relative to dissipation in the system, which requires (1) high pump and seed power, (2) a strongly resonant nonlinear multimode cavity, and (3) a method to tune the dissipation (Q factor) for different frequency modes. In addition to free space optical parametric oscillators (OPOs), on chip OPOs may offer a platform to realize the effects described here with compact form factor [91]. Recent advances in the integration of lithium niobate photonics with ultra high Q whispering gallery mode resonators [92, 93], for instance, may provide the necessary elements to generate cascading nonlinear processes, though intrinsic losses (particularly at the idler frequency) will need to be minimized.

The effects we have described here do not depend on specific spectral ranges for the pump, signal, and idler modes. Depending on the platform and material, a higher frequency mid-IR idler mode could be used instead, potentially with lower losses at the expense of a shorter comb. Furthermore, an essential part of our approach is Q factor engineering, which allows one to tune the length of the frequency comb, relative amplitudes of the different modes, and which modes are squeezed/correlated. Experimentally, this Q factor engineering can be achieved by using photonic crystals that provide frequency-tunable filters for coupling into and out of the cavity.

Our work establishes the mechanism of cascaded nonlinear optical processes as a method to generate frequency combs that exhibit bright squeezing and quantum correlations over a broad (and tunable) spectral range. We envision future appli-

cation of the concepts described here to tunable squeezed light sources, multimode entanglement for sensing and quantum computing protocols, and much more.

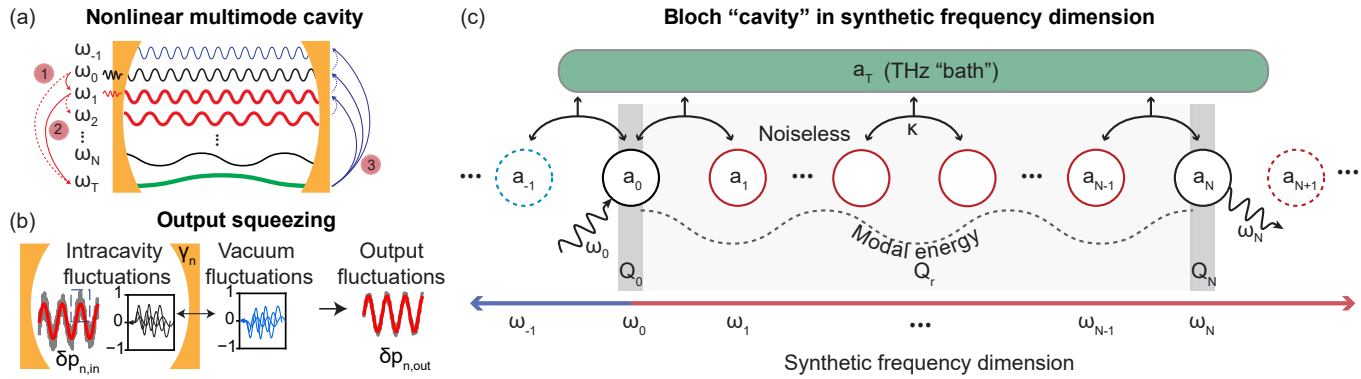

Figure 3-1: **Squeezing in a multimode cavity with THz-mediated cascaded three wave mixing.** (a) Cascading infrared (IR) orders are resonant in a multimode cavity and undergo three wave mixing (TWM) mediated by a terahertz (THz) mode, creating a frequency comb (red) with modes separated by the THz frequency ω_T (green). The cascade starts with a single TWM process wherein a pump photon at ω_0 amplifies a seed photon at ω_1 (solid line) and simultaneously creates an idler photon (THz, dashed line) (1). Subsequently, the amplified mode at ω_1 initiates cascading downconversion processes, now seeded by the THz idler photon (2). Concomitantly, THz photons can also initiate upconversion processes that repopulate the IR orders (3). By shaping the Q factor distribution of the cavity (e.g., through a frequency-dependent coupler), the modes blueshifted relative to the pump frequency ω_0 can be suppressed, biasing downconversions that create THz photons. Through parametric squeezing enabled by the strong nonlinear rates, the multimode cavity can create above-threshold output squeezing in frequency mode(s) that are separated from the coherent pump mode by multiple idler photons. (b) Shown for a single mode, the output squeezing emerges due to destructive interference between the intracavity fluctuations and vacuum shot noise on the output facet of the cavity outcoupling mirror. (c) Strong squeezing requires strong nonlinear energy flow, which creates a kind of nonlinear tight binding system in frequency space. The system is bounded by low Q modes at frequencies $\omega_{0,N}$, resulting in a frequency space cavity (modes within the cavity generally have high Q factors). Excitation of counter-propagating Bloch modes in this cavity creates an interference pattern that is observable in the modal energy distribution.

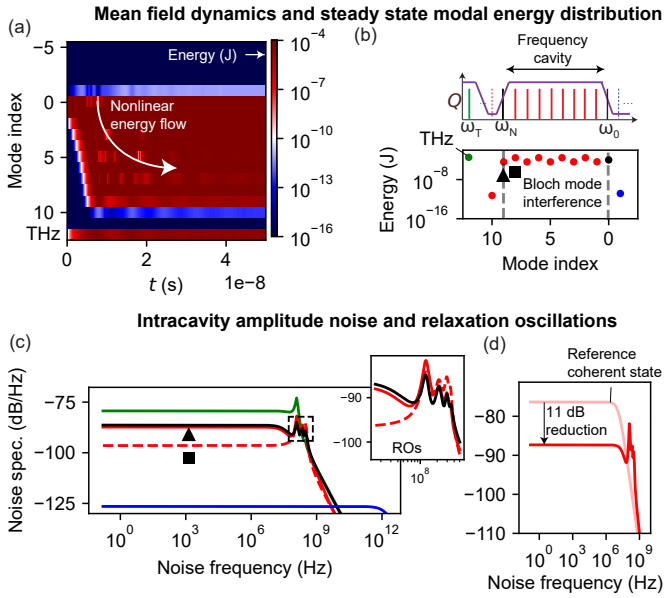

Figure 3-2: **Intracavity dynamics and noise due to strong cascaded nonlinear interactions.** (a) Q factor shaping (through the use of frequency-dependent couplers) permits the creation of frequency combs containing only redshifted modes relative to the pump mode a_0. The temporal dynamics feature Bloch waves that propagate through frequency space, establishing the steady state interference pattern in intracavity modal energy. (b) Q factors for the different frequency modes and quasi-periodic modal energy distribution in frequency space enabled through cascaded nonlinear interactions. Green denotes the (THz) idler mode a_T, red denotes infrared cascading orders $a_{n>0}$, black denotes the pump mode a_0, and blue denotes blueshifted modes $a_{n<0}$ (suppressed in the present system). The dashed lines indicate the boundaries of the cavity in the synthetic frequency dimension. (c), (d) Intracavity relative intensity noise spectra for modes a_T (green), $a_{N-1,N}$ (red, ▲ for a_N and ■ for a_{N-1}), a_0 (black), and a_{-1} (blue). The blueshifted mode is a coherent state that is approximately decoupled from the nonlinear interactions due to its low Q factor. The pump and IR cascading orders have low frequency noise that lies far below the reference coherent state defined by a state with identical decay channel but no nonlinear coupling. However, these modes feature strong GHz relaxation oscillations (ROs). Multiple relaxation oscillation peaks (around the nonlinear rate $|\kappa a_T|$) are present due to the TWM processes occurring in the multi-resonant cavity. In these simulations, the pump and seed wavelengths are $\lambda_{0,1} = 1064, 1068$ nm (so that $\omega_T = 2\pi \cdot 1.06$ THz). $N = 9$ cascading orders are simulated, along with two low Q "padding modes" on either side of the frequency space cavity. Q factors used are: $Q_r = 10^7$ (redshifted modes in frequency space cavity), $Q_0 = Q_N = 10^5$ (frequency mirrors), $Q_b = 10^2$ (blueshifted modes), and $Q_T = 10^4$ (THz idler mode). The nonlinear strength is $\kappa = 4.70$ s^{-1} and the input pump and seed powers are $|s_{0,1}|^2 = 1$ MW.

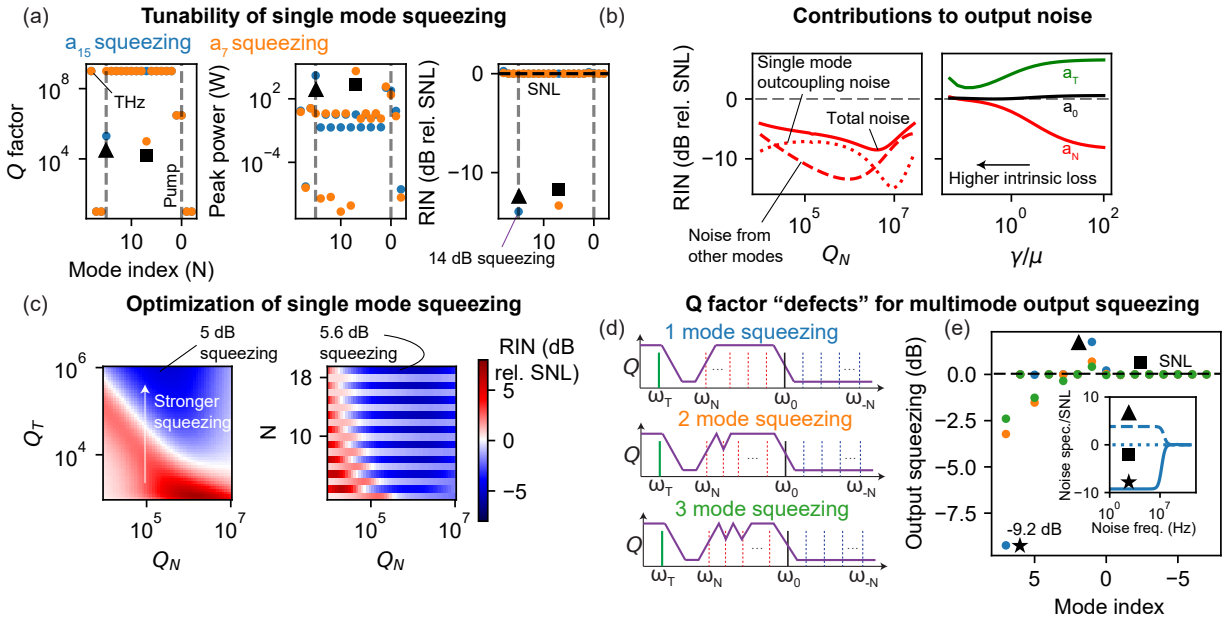

Figure 3-3: **Single and multimode output noise squeezing.** (a) Using a similar cavity design to that presented in Fig. 3-2, single frequency modes in the synthetic frequency dimension can be squeezed in output noise. Here, we simulate $N = 15$ cascading orders, and the mode with low Q is squeezed. Dashed lines demarcate the boundaries of the frequency space cavity. We plot the steady state output power in the modes; due to their low Q, the squeezed modes have the highest power outside the cavity. The remaining IR modes show an interference pattern in steady state power characteristic of the Bloch interference phenomenon in Fig. 3-2. The terahertz mode a_T also has high power, while modes outside the frequency space cavity are very leaky and negligibly occupied in the steady state. The modes that are designed to have low Q are the only ones to show significant departure from the shot noise limit (SNL), demonstrating intensity noise squeezing exceeding 10 dB. In these simulations, $Q_0 = 3 \times 10^6, Q_N = 2 \times 10^5, Q_r = Q_T = 10^9$ and $\kappa = 14.1\ \mathrm{s}^{-1}$. (b), (c) The single mode output squeezing (here for mode a_N) can be maximized by optimizing multiple parameters simultaneously. Here, we show that higher Q_T and lower intrinsic loss generates stronger squeezing due to stronger nonlinear energy flow. A larger number of modes (N) can also help increase squeezing, though too many modes can make the noise contribution from modes $a_{k\neq N}$ significant (red dashed curve in (c)). Lastly, an optimal Q_N exists (with all parameters held equal) to maximize squeezing. Roughly, this Q_N maximizes destructive interference with vacuum shot noise as per condition (1) (red dotted curve in (c)). In (b), (c), $Q_r = 10^8$ and μ/γ denotes the ratio of intrinsic loss to the outcoupling rate. (d), (e) By shaping the Q factor profile of the multimode cavity, specifically by introducing multiple Q factor "defects," output squeezing can be obtained for multiple frequency modes. Here, $N = 7$ modes are simulated. The bandwidth for squeezing in the inset is around 100 MHz, but can be optimized to > 1 GHz by enabling stronger nonlinear rates.

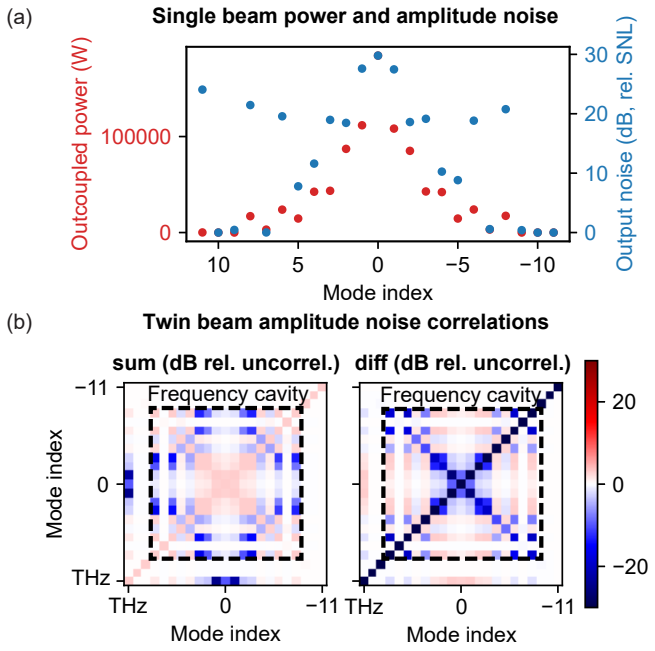

Figure 3-4: **Twin beam correlations.** (a) Single beam outcoupled power and (DC) output noise. (b) Twin beam intensity sum and difference fluctuations $\langle \delta n_i \pm \delta n_j \rangle$ normalized to the uncorrelated twin beam noise. Despite certain modes being strongly antisqueezed in (individual) output amplitude noise, strong correlations between multiple pairs of modes significantly reduce the twin beam noise. These correlations span the dimension of the frequency cavity and may point towards the possibility of long-range entanglement in a synthetic frequency dimension. Simulation parameters are $Q_0 = Q_N = Q_r = Q_b = 3 \times 10^6, Q_T = 10^5, \kappa = 3 \times 10^{-4}$ J$^{-1/2}$, and $|s_0|^2 = 1$ MW, $|s_1|^2 = 100$ W. All noises are computed at noise frequencies much lower than the cavity bandwidth.

Chapter 4

Future directions

In this thesis, I have described two theoretical proposals for generating broadband and spectrally tunable bright intensity noise squeezing in single and multiple optical modes. This work stands as a distinct paradigm shift from most works that have considered vacuum squeezing and thus opens up many exciting quantum applications. For example, the strong intracavity squeezing we have shown through the mechanism of nonlinear dissipation could enable new systems in cavity quantum electrodynamics characterized by strong interactions with macroscopic "bright" quantum light. The squeezing at mid-IR and THz frequencies described in Chapter 2 suggests the possibly of developing quantum-enhanced biochemical sensors, considering that many molecules have important spectral signatures at these frequencies. Finally, the spectrally tunable single- and multimode squeezing I have shown through cascaded nonlinear optical processes could enable bright squeezing in frequency combs for quantum metrology and noise-reduced frequency multiplexing in quantum optics.

I am actively investigating multiple avenues related to these works. Here, I briefly describe some of my active theoretical and experimental projects. On the theory side:

1. For practical applications in metrology, linewidth is an important consideration for light sources. For both mechanisms of single-mode and multimode squeezing considered here, it would be of interest to characterize the phase noise of the squeezed modes. Note that it is not necessarily the case that phase noise will

be antisqueezed if the intensity noise is squeezed, since the systems we consider here (such as the laser) are not Heisenberg-limited.

2. We saw in Chapter 3 that intracavity squeezing was difficult due to the presence of heavily multimoded relaxation oscillations. Techniques like nonlinear dissipation could be incorporated into the system to generate multimode intracavity squeezing. Furthermore, we saw that output squeezing can decrease significantly as the number of squeezed modes increases. This is because of stronger output coupling noise between the squeezed modes. To overcome this, I am investigating the generalization of nonlinear dissipation to multimode squeezing. This may require engineering multiple sharp dispersive resonances at the frequencies of the squeezed modes.

3. The multimode cavity system considered in Chapter 3 is the ideal platform to investigate non-Hermitian physics and topological effects in a synthetic frequency dimension. I am actively investigating topologically-protected quantum states that this system can sustain in both the few-photon and many-photon regimes.

On the experimental side, I am actively working on an experiment designed to probe some of the theoretical predictions made in Chapter 3. Currently, we are working towards showing an enhancement in the terahertz idler mode generation efficiency beyond the Manley-Rowe limit, as described in [76]. This is the first step towards realizing strong intermodal nonlinear coupling in our multimode cavity that will be essential to mold the quantum noise properties of the system as described in Chapter 3.

Appendix A

Appendix for strong intensity noise squeezing in semiconductor lasers using nonlinear dissipation

A.1 Heisenberg-Langevin equations of motion

The Hamiltonian of a simple two-band semiconductor can be writen as

$$H_{\mathrm{SC}} = \sum_q (\epsilon_g^{(0)} + \epsilon_{e,q}) c_q^\dagger c_q + \sum_q \epsilon_{h,q} h_q^\dagger h_q + V_{\mathrm{int}}. \tag{A.1}$$

Here, c_q and h_q are the fermionic annihilation operators for conduction-band electrons and valence-band holess at momentum q. They satisfy the fermionic commutation relations $\{c_q, c_{q'}^\dagger\} = \delta_{qq'}$, and likewise for h_q. Additionally, $\epsilon_g^{(0)}$ is the unrenormalized bandgap energy which separates the two bands at zero momentum. Also note that the sums $\sum_q$ are intended to note a sum over all electron states q, including momentum, spin, and anything else that might be relevant. Finally, V_{int} represent interactions (collisions between electrons, interactions of the electron with the lattice, etc.). We will not need to consider the effects of this term, but its presence will lead to effects such as collision-induced equilibration of carriers within a band, relaxation of carriers from the upper band to the lower band, etc. Interactions can also lead to some shifts

in the gain spectrum induced by carrier screening and band-gap renormalization.

Now, we would like to introduce a single mode Kerr nonlinear cavity which has frequency ω_0 and annihilation operator a, so that the Hamiltonian of the cavity is $H_{\text{cavity}} = \omega_0 a^\dagger a \left(1 + \beta a^\dagger a\right)$ with β the per-photon Kerr nonlinearity. In order to describe lasing, the cavity should interact with the semiconductor gain medium through its dipole moment. We can define analogs of the atomic raising/lowering operators $\sigma_\pm$ for each electron label q as $\sigma_q \equiv c_q h_q$. Then, in the rotating wave approximation (which assumes the light-matter coupling between the light and semiconductor is weak), the interaction between cavity and semiconductor is

$$H_{\text{int}} = \sum_q \left(g_q a \sigma_q^\dagger + g_q^* \sigma_q a^\dagger\right). \tag{A.2}$$

Then the Hamiltonian of the full laser is the sum of the contributions $H = H_{\text{SC}} + H_{\text{cavity}} + H_{\text{int}}$. Our goal then is to write equations of motion for quantities of interest, and then solve these equations for steady state, transient, and noise properties of the laser. To do so, we will now write Langevin equations of motion for the semiconductor laser. This amounts to computing the Heisenberg equations of motion for the operators of interest, adding the relevant pumping and damping terms, and finally computing the correlations between the Langevin forces which results to describe noise behavior.

For the polarization operator, we find

$$\dot{\sigma}_q = -i\omega_q \sigma_q - \gamma_\perp \sigma_q + i g_q a (n_{e,q} + n_{h,q} - 1) + f_q, \tag{A.3}$$

where ω_q is the energy difference between the valence and conduction bands for state q. We see that σ_q oscillates in the same way that σ_i does for an atomic gain medium. Additionally, we see that the quantity in parentheses (which we shall define as d_q) in the second term acts like the inversion in an atomic gain medium. Specifically, the occupation operators for the electrons and holes can both takes values between 0 and 1. For a completely unexcited state ($n_e = n_h = 0$), the grouped quantity is $d_q = -1$.

For a completely excited state ($n_e = n_h = 1$) we have $d_q = 1$. Thus d_q can be thought of as the population inversion for each electron state q.

For the cavity photon annihilation operator,

$$\begin{aligned}\dot{a} &= -i\omega_0 \left(1 + \beta a^\dagger a\right) a - \frac{\kappa}{2} a - i \sum_q g_q^* \sigma_q + f_a \\ &= -i\omega_0 a \left(1 + \beta a^\dagger a\right) a - \frac{\kappa}{2} a + \frac{a}{\gamma_\perp} \sum_q |g_q|^2 \mathcal{D}_q d_q + f_a,\end{aligned} \tag{A.4}$$

where κ is the cavity number/energy damping rate, $\mathcal{D}_q \equiv \frac{\gamma_\perp}{i(\omega - \omega_q) + \gamma_\perp}$ and f_a is the Langevin force for the annihilation operator. In the second line, we adiabatically eliminated the polarization. Note that β represents the per-photon Kerr nonlinear strength.

Lastly, for the electron occupation operator,

$$\dot{n}_{e,q} = \Lambda_{e,q}(1 - n_{e,q}) - B_q n_{e,q} n_{h,q} - \gamma_\parallel n_{e,q} - \gamma_e (n_{e,q} - (n_{e,q})_0) + i g_q^* a^\dagger \sigma_q - i g_q \sigma_q^\dagger a + F_{e,q}. \tag{A.5}$$

In order from left to right, the terms are

- **Population pumping.** This is the pump rate due to carrier injection. When summing over this term, we get the actual pump rate I at which free carriers are injected.

- **Loss due to spontaneous emission.** Excited carriers can be lost due to spontaneous emission. Since different q can have different energy splittings, one of these spontaneous emission events will not necessarily be into the laser mode of interest. The coefficient B_q is the rate for a particular momentum state q.

- **Nonradiative decay of population.** This term represents the rate at which exited carriers become unexcited in a manner which is proportional to the population (e.g., due to phonon emission).

- **Carrier-carrier relaxation.** This term represents relaxation to the equilibrium value $(n_{e,q})_0$ within a band. The fact that γ_e tends to be very large

compared to other relaxation rates allows one to make the so-called "quasiequilibrium" approximation in which each band acquires a Fermi-Dirac distribution. Moreover, because this term only redistributes carriers to different q within the same band, it does not have an effect on the total inverted population. Thus, when summing this term over electron states, it vanishes.

- **Population depletion by stimulated emission into cavity mode.** This is the only term that can be derived from the Hamiltonian written above. This is the term that causes the population of excited states to deplete when stimulated emission occurs.

Now, we identify

$$G(N)(1 - i\alpha_L) \equiv \frac{2}{\gamma_\perp} \sum_q |g_q|^2 d_q \mathcal{D}_q \tag{A.6}$$

$$\Gamma(N) \equiv \gamma_\parallel N + \frac{1}{V} \sum_q B_q n_{e,q} n_{h,q} \tag{A.7}$$

$$N \equiv \sum_q n_{e,q}. \tag{A.8}$$

where the linewidth enhancement factor $\alpha_L \equiv \frac{d\chi_r/dN}{d\chi_i/dN}$, with $\chi = \chi_r + i\chi_i$ the susceptibility of the active material [94]. We can now identify the resonance frequency using $a \equiv \alpha e^{i\phi}$ and $\dot{\phi} = \frac{1}{2}\frac{d}{dt}\ln\left(\frac{a}{a^\dagger}\right) = \frac{\dot{a}}{2a} - \frac{\dot{a}^\dagger}{2a^\dagger}$, showing that

$$\omega_0 \to \omega_0 \left(1 + \beta n + \frac{\alpha_L}{2\omega_0} G(N)\right), \tag{A.9}$$

so that the "carrier nonlinearity" is identified as $\sigma \equiv \alpha_L G_N / 2\omega_0$. With these substitutions and neglecting the effects of spontaneous emission, the Heisenberg-Langevin equations in the main text are obtained.

Here, we neglected any frequency-dependent phase shifts imparted by the Fano mirror. These can be rigorously incorporated into the Heisenberg-Langevin equations using coupled mode theory, as we do below in Sec. A.4. The result is a phase shift $\tan^{-1}(\delta(\omega)/\gamma)$, where $\delta(\omega)$ represents the detuning from the Fano resonance and 2γ

the width of the Fano resonance. We assume the second cavity mirror (back reflector) is broadband and imparts no phase shift. The effect of including the Fano mirror's phase shift is to make the resonance frequency no longer analytically solvable given n, N using Eq. A.9. Instead, it must be solved numerically. However, we find that the effect of this dispersive phase shift is negligible over the detunings we consider: sweeping across the Fano resonance gives a deviation from the prediction of Eq. A.9 of at most 0.02γ, likely from the broad width we assume for the Fano resonance under the adiabatic approximation.

A.1.1 Carrier equation of motion under optical excitation

In the case of free carrier excitation due to optical pumping, the mean field carrier equation of motion derived from the Heisenberg-Langevin formalism reads [1]

$$\dot{N} = \frac{\eta P_p}{\hbar\omega_p V_p} - \gamma_{\|} N - nG(N), \tag{A.10}$$

where η is the pump efficiency, P_p the pump power, $\hbar\omega_p$ the energy of a pump photon, and V_p the pump volume. Assuming a pump volume V_p on the order of the active region volume and excitation by a near-IR source (around 800 nm), typical pump powers are on the order of tens of mW for examples considered in the main text with pump currents on the order of tens of mA.

A.1.2 Estimation of per-photon Kerr nonlinearity β

We briefly describe how the per-photon Kerr nonlinearity β can be estimated. Previous work has derived the per-photon Kerr nonlinearity from a quantum mechanical Hamiltonian approach [28]:

$$\beta = \frac{3\hbar\omega_0}{8\epsilon_0^2} \int \chi^{(3)}(\mathbf{r}) |\mathbf{u}(\mathbf{r})|^4 d^3\mathbf{r}, \tag{A.11}$$

where the electric field profile is normalized as $\int |\mathbf{u}(\mathbf{r})|^2 \epsilon_r(\mathbf{r}) d^3\mathbf{r} = 1$. To get an estimate of achievable β, we consider a buried heterostructure laser with GaAs gain

and $Al_{0.34}Ga_{0.66}As$ cladding. The active region has dimensions 0.1 μm $\times$ 5 μm $\times$ 1 mm, the lasing frequency is near the bandgap of GaAs, $\omega_0 = 2.16 \times 10^{15}$ rad/s, and the refractive indices of GaAs and $Al_{0.34}Ga_{0.66}As$ are 3.6051 and 3.3734 respectively. We take $n_2 \approx -10^{-16}$ m^2/W for $Al_{0.34}Ga_{0.66}As$ [95]. We solve Maxwell's equations in the core and cladding using a slab waveguide model, obtaining a confinement factor $\Gamma \approx 0.3$ and per-photon Kerr nonlinearity $\beta \approx -6 \times 10^{-10}$.

A.2 Mean-field dynamics: bistability and self-pulsing

A.2.1 Bistability due to Kerr nonlinearity

Here, we quantify the bistability boundaries that arise when intensity-dependent loss is present. As shown in Fig. 2, this bistability correlates with the phenomenon of self-pulsing and demarcates an unstable region in the S-curve for the laser. Its boundaries can be found by noting that, in the steady state,

$$\begin{aligned} I(n) &= \gamma_{\|} N(n) + n G_N \left(N(n) - N_{\text{trans}}\right) \\ N(n) &= \frac{\kappa(n)}{G_N} + N_{\text{trans}}. \end{aligned} \tag{A.12}$$

The bistability boundaries (in pump I) are those values $I(n)$ for which $dI/dn = 0$, for which we require

$$\frac{dI}{dn} = 0 \implies \kappa_n \left(\frac{\gamma_{\|}}{G_N} + n \right) + \kappa(n) = 0. \tag{A.13}$$

One can see, for example, that in the absence of intrinsic loss, n_c, the point of zero loss, satisfies this condition, since $\kappa_n(n_c) = \kappa(n_c) = 0$.

A.2.2 Onset and cessation of self-pulsing

Self-pulsations begin when relaxation oscillations become undamped, $\Gamma_1 < 0$ and $\Omega_R^2 > 0$ (in the initial steady state solution). They do not, however, persist throughout the entire region where $\Gamma_1 < 0$, as shown in Fig. 2 of the main text. When the laser

begins at the left edge of bistability in the S-curve (as in Fig. 2b) at steady state, the pulsations are transient and eventually collapse to the steady state solution at the center of the Fano resonance with minimum loss at photon number n_c (this is the leftmost point of bistability). Note that the laser began at the second photon number n^* (low intensity branch) that corresponds to the same pump power as photon number n_c. Eventually, we sweep through initial steady state photon numbers within the region of instability (still within bistable operation) that is not normally accessible by pumping directly from threshold. When the right edge of bistability is finally crossed, the laser enters the region with $\kappa_n > 0$, characterized by heavily damped relaxation oscillations and intensity noise squeezing. When pumping from threshold, the laser jumps from the low intensity to high intensity branch at the right bistable edge.

A.2.3 Pulse characteristics in self-pulsing regime

The self-pulsations demonstrate an interesting behavior in pulse shape, as shown in Fig. A-1. The initial sharp rise in the pulse profile is due to the undamping of relaxation oscillations, and its timescale is thus set by $1/|\Gamma_1|_{\max} \approx 1/|n\kappa_n|_{\max}$ ($\mathcal{O}(1)$ ps in our simulations). The same timescale characterizes the final drop in pulse power. In between these two features, two further timescales are at play. The decay after peak pulse power is initially very fast ($\mathcal{O}(1)$ ps) due to the strong damping of relaxation oscillations in the $\kappa_n > 0$ region. The decay slows as the photon number approaches n_c, governed by Γ_1 evaluated at $n \approx n_c$. The final feature also sets the longest timescale for the pulse. It is a plateau near $n \approx n_c$ that emerges from "quasi" steady state conditions. The carrier density can be calculated by solving the carrier equation of motion in the steady state as

$$N \approx \frac{I_0 + n_c G_N N_{\text{trans}}}{\gamma_{\|} + n_c G_N}, \tag{A.14}$$

where I_0 denotes the (fixed) pumping rate. Notice here that for $n < n^*$, $N < N(n_c)$, so that $G(N) < \kappa(n)$ as the photon number drops below n_c and approaches the

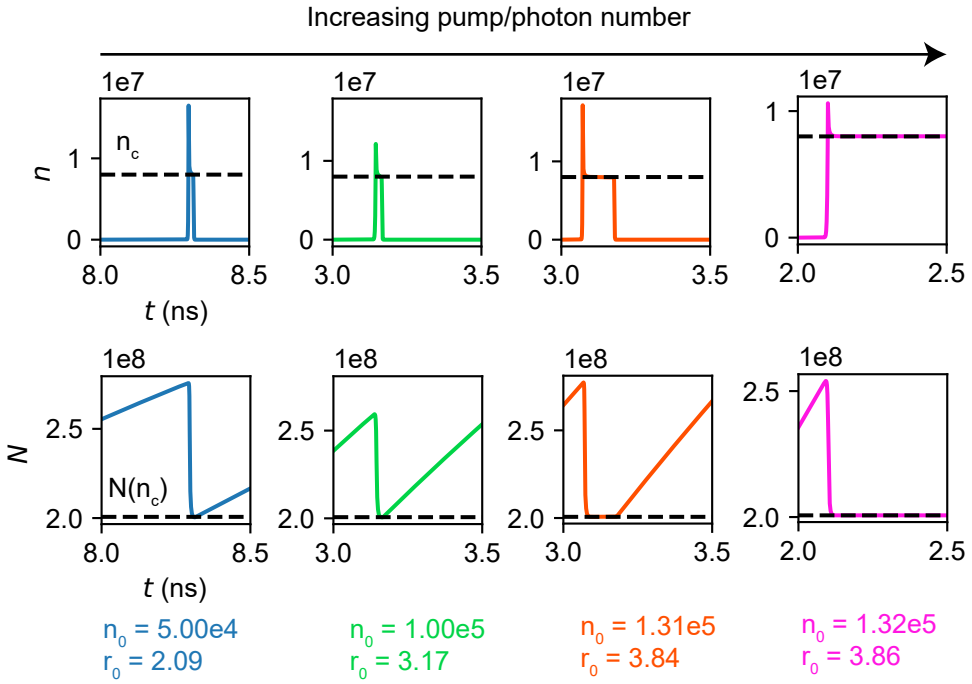

Figure A-1: **Evolution of the pulse profile for carrier density and photon number from the self-pulsing to collapsed pulse regimes.** As the initial photon number n_0 approaches the left bistable edge, the pulse plateaus for longer at the center of the Fano resonance. Thus, the effective width of the pulse is dynamic within the regime over which self-pulsing occurs, depending on the initial state's proximity to the left bistable edge. Once the left bistable edge is crossed, the pulse collapses to a CW solution at higher photon number than the initial state. Here, r_0 denotes the initial pumping rate relative to threshold.

point where the pulsing continues ($\Gamma_1 < 0$). The timescale for the plateau is then given by $\tau_p = 1/|G(N) - \kappa(n_c)|$. Notice that $N \to N_c, \tau_p \to \infty$ as the initial steady state photon number $n_0 \to n^*$. When $n_0 = n^*$, the pulsations are transient and the laser approaches a steady state at $n_0 = n_c$, as shown in Fig. A-1. For $n_0 \approx n^*$, the plateau changes based on the initial steady state (i.e. pumping rate) and can approach timescales of tens to hundreds of ps.

The peak pulse power is more difficult to predict, depending on the initial fluctuation from steady state. However, it must occur at $n > n_c$ to saturate the pulse and begin its decline.

The pulse repetition rate is set by the carrier density recovery timescale when the pulse is off. During this time, the photon number $n \approx 0$, so that the mean-field dynamics of carrier density are given by

$$N(t) = \left(N_{\min} - \frac{I}{\gamma_\parallel}\right) e^{-\gamma_\parallel t} + \frac{I}{\gamma_\parallel}, \tag{A.15}$$

where I denotes the pump current and $N_{\min}$ the minimum carrier density. If $\Delta N = N_{\max} - N_{\min}$ is the difference in carrier density at the pulse maximum and minimum, the period between pulses is given roughly by

$$T_{\text{rep}} \approx \frac{1}{\gamma_\parallel} \ln\left(\frac{I/\gamma_\parallel - N_{\min}}{I/\gamma_\parallel - N_{\max}}\right). \tag{A.16}$$

For the system parameters in the main text, $T_{\text{rep}} \sim 10$ ns (100 MHz repetition rate).

A.3 Intensity noise

A.3.1 Langevin force correlators

In this section, we derive the photon number correlator in the presence of two-photon absorption (TPA). We begin with the equation of motion for photon number probabilities in the presence of TPA only, $\dot{p}_n = -\frac{\alpha_{\text{TPA}}}{2} n(n-1)p_n + \frac{\alpha_{\text{TPA}}}{2}(n+1)(n+2)p_{n+2}$, where p_n denotes the probability of having n photons inside the laser cavity. Thus,

$$\begin{aligned}\langle \dot{n} \rangle &= \sum_j j \dot{p}_j \\ &= -2\alpha_{\mathrm{TPA}} \sum_j j(j-1) p_j \\ &= -\alpha_{\mathrm{TPA}} [\langle n^2 \rangle - \langle n \rangle].\end{aligned} \tag{A.17}$$

The RHS reduces to $-\alpha_{\mathrm{TPA}} \langle n \rangle^2$ assuming mean field theory, $\Delta n \ll \langle n \rangle$, recovering the equation of motion $\dot{n} = -\alpha_{\mathrm{TPA}} n^2$. Using the generalized Einstein relation, the correlator is $\langle 2D_{nn} \rangle = \frac{d}{dt}\langle n^2 \rangle - 2\langle n D_n \rangle$, where we express $\dot{n} = D_n + F_n$, with D_n a diffusion term and F_n a Langevin force. Thus

$$\begin{aligned}\langle 2D_{nn} \rangle &= \left(\sum n^2 \dot{p}_n \right) + 2\alpha_{\mathrm{TPA}} \langle n^3 - n^2 \rangle \\ &= -\alpha_{\mathrm{TPA}} \langle n(n-1)^2 \rangle + 2\alpha_{\mathrm{TPA}} \langle n^2 (n-1) \rangle \\ &\approx 2\alpha_{\mathrm{TPA}} \langle n \rangle^2,\end{aligned} \tag{A.18}$$

again assuming mean field theory. Allowing for one-photon gain and loss, $\langle 2D_{nn} \rangle = 2\kappa n + \alpha_{\mathrm{TPA}} n^2$. The other nonzero diffusion coefficients are $\langle F_N^\dagger F_N \rangle = \langle 2D_{NN} \rangle = \epsilon I + R_{sp} n + \gamma_\parallel N$, $\langle F_N^\dagger F_n \rangle = \langle 2D_{Nn} \rangle = -Rn$, $\langle F_\phi^\dagger F_\phi \rangle = \langle 2D_{\phi\phi} \rangle = R_{sp}/2n$ where $R_{sp} \approx G(n, N)$ denotes the rate of spontaneous emission into the cavity mode, $R_{abs} \approx 0$ denotes the rate of absorption (negligible above threshold), $R = R_{sp} + R_{abs}$, and $\epsilon = 0$ (1) for quiet (noisy) pumping. These correlators can be derived by computing the Einstein diffusion coefficients [2] and give rise to nonzero fluctuations in n, N about their steady state values. For intracavity noise calculations in the main text, pump noise is always included. Output noise calculations are performed for both noisy and quiet pumping schemes.

A.3.2 Analytic intensity noise spectra and Fano factor expressions

In this section, we provide a linearization of the semiconductor laser rate equations in the presence of various nonlinearities and calculate relative intensity noise using this formalism. We obtain

$$\begin{aligned}\delta\dot{n} &= -\left(\kappa_n n + \frac{pG_0}{2(1+p)}\right)\delta n + n\left(G_N - \kappa_N\right)\delta N + F_n - n\kappa_\omega F_\phi \\ \delta\dot{N} &= -\left(\frac{G_0(1+p/2)}{1+p} - I_n\right)\delta n - \left(G_N n + \gamma_\parallel\right)\delta N + F_N.\end{aligned} \tag{A.19}$$

where $p = n/n_{\text{sat}}$ denotes the saturation fraction for photon number and $I_n \equiv dI/dn$ denotes carrier generation by TPA. Note that G_0, G_N implicitly include the effects of gain saturation, $G_{0,N} \to G_{0,N}/\sqrt{1+p}$. Results in the main text assume $p, I_n \to 0$.

For simplicity of notation, we will introduce $a = nG_N + \gamma_\parallel, b = n\left(G_N - \kappa_N\right), c = G_0\frac{1+p/2}{1+p} - I_n, d = n(\kappa_n - G_n), \Gamma_1 = a+d, \Omega_R^2 = ad+bc$. Note that Ω_R^2 denotes the approximate relaxation oscillation frequency and Γ_1 the decay of relaxation oscillations. Fourier transforming the linearized rate equations,

$$\begin{bmatrix} -i\Omega + d & -b \\ c & -i\Omega + a \end{bmatrix}\begin{bmatrix}\delta n(\Omega) \\ \delta N(\Omega)\end{bmatrix} = \begin{bmatrix} F_n - n\kappa_\omega F_\phi \\ F_N \end{bmatrix}, \tag{A.20}$$

yielding

$$\begin{bmatrix}\delta n(\Omega) \\ \delta N(\Omega)\end{bmatrix} = \frac{1}{-\Omega^2 + (ad+bc) - i\Omega(a+d)}\begin{bmatrix}(-i\Omega + a)\left(F_n - n\kappa_\omega F_\phi\right) + bF_N \\ -c\left(F_n - n\kappa_\omega F_\phi\right) + (-i\Omega + d)F_N.\end{bmatrix} \tag{A.21}$$

The intensity noise spectrum is then

$$\langle \delta n^\dagger(\Omega)\delta n(\Omega)\rangle = \frac{(\Omega^2 + a^2)[\langle 2D_{nn}\rangle + n^2\kappa_\omega^2\langle 2D_{\phi\phi}\rangle] + b^2\langle 2D_{NN}\rangle + 2ab\langle 2D_{Nn}\rangle}{(\Omega^2 - \Omega_R^2)^2 + \Omega^2\Gamma_1^2}. \tag{A.22}$$

As a side note, ignoring the effect of Kerr nonlinearity but including dispersive loss and the associated amplitude-phase coupling, we see that RIN can be reduced by a factor $(1+\kappa_\omega^2)/(1-\alpha_L\kappa_\omega/2)^2 \to 1/(1+\alpha_L^2)$ if the slope κ_ω is chosen appropriately, in agreement with earlier work on amplitude-phase decorrelation (where intensity noise is reduced somewhat at the expense of an increase in phase noise) [25]. However, this method leads to frequency selective squeezing, as opposed to the type of broadband squeezing we consider here.

We compute the Fano factor from Eq. A.22 using the integrals

$$I_1 = \int_0^\infty \frac{1}{(\omega^2-x^2)^2+y^2}d\omega = \frac{\pi}{4y}\frac{\sqrt{2x^2+2\sqrt{x^4+y^2}}}{\sqrt{x^4+y^2}}$$
$$I_2 = \int_0^\infty \frac{\omega^2}{(\omega^2-x^2)^2+y^2}d\omega = \frac{\pi}{4}\frac{\sqrt{-2x^2+2\sqrt{x^4+y^2}}}{\sqrt{x^4+y^2}} + x^2 I_1,$$

where $x, y \in \mathbb{R}$. With $x^2 = \Omega_R^2 - \frac{\Gamma_1^2}{2}, y^2 = \Gamma_1^2\left(\Omega_R^2 - \frac{\Gamma_1^2}{4}\right)$, we have $I_1 = \frac{\pi}{2\Gamma_1\Omega_R^2}, I_2 = \frac{\pi}{2\Gamma_1}$. Thus, the Fano factor reads

$$F = \frac{1}{2n\Gamma_1\Omega_R^2}\left([\langle 2D_{nn}\rangle + n^2\kappa_\phi^2\langle 2D_{\phi\phi}\rangle](\Omega_R^2+a^2) + \langle 2D_{Nn}\rangle ab + \langle 2D_{NN}\rangle b^2\right) \quad \text{(A.23)}$$

We now consider limiting expressions for F in various limiting cases:

1. For weak Kerr and carrier nonlinearities, $\kappa_n, \kappa_N \to 0$, we have $F \to 1+\kappa/(nG_N)$ when pumping far above threshold, recovering linear behavior. When n becomes large far about threshold, the Fano factor approaches 1, resulting in Poissonian (coherent) statistics.

2. For strong Kerr nonlinearity but weak carrier nonlinearity, $n\kappa_n \gg \kappa_0, n|\kappa_N|, \gamma_\parallel, G_N$, the Fano factor $F \to \kappa/(n\kappa_n)$ for large n, resulting in squeezing when $n\kappa_n > \kappa$.

3. For strong carrier nonlinearity but weak Kerr nonlinearity, $n|\kappa_N| \gg \kappa_0, n|\kappa_n|, \gamma_\parallel$, we have $F \to \kappa/(nG_N) + G_N/|G_N-\kappa_N| \to G_N/|G_N-\kappa_N|$ for large n. The

carrier nonlinearity reduces dependence of the rate of change of intensity fluctuations on carrier fluctuations ($G_N \to G_N - \kappa_N$), lowering the relaxation oscillation frequency Ω_R^2 while leaving the damping of these oscillations unchanged. This can amplify low-frequency intensity noise slightly.

4. For simultaneously strong Kerr and carrier nonlinearities, $n|\kappa_{n,N}| \gg \kappa_0, \gamma_\parallel$,

$$F \to \frac{\kappa}{n|G_N + \kappa_n|}\left(1 + \frac{nG_N^2}{n\kappa_n G_N + |G_N - \kappa_N|\kappa}\right). \tag{A.24}$$

Roughly, this expression can be broken into Kerr nonlinearity (first term) and carrier nonlinearity (second term) contributions. The former describes squeezing via increased Ω_R^2 and damping of relaxation oscillations due to "sharp" intensity-dependent loss, while the latter reduces intensity noise-carrier noise coupling and thus Ω_R^2. Kerr and carrier nonlinearities may therefore have competing effects, leading to interesting steady state and noise fluctuation behavior.

A.3.3 Noise reduction using two photon absorption (TPA)

Two photon absorption (TPA), though not a dispersive loss, is weakly nonlinear in photon number and thus may be expected to permit some squeezing in intensity noise. When TPA is present, for large n,

$$F \to \frac{3\kappa}{2n(G_N + \alpha_{\mathrm{TPA}})}\left(1 + \frac{G_N}{\alpha_{\mathrm{TPA}} + \kappa/n}\right), \tag{A.25}$$

where $\alpha_{\mathrm{TPA}} = \kappa_n$. The minimum achievable Fano factor is $3/4$, obtained when $\kappa_0/n \ll \alpha_{\mathrm{TPA}} \ll G_N$ (here κ_0 denotes linear background loss). To obtain the TPA coefficient α_{TPA}, we use the relationship between intensity I and photon number $I \sim n\hbar\omega c/V$, so that $\alpha_{\mathrm{TPA}} \sim 2\hbar\omega c L\beta_{\mathrm{TPA}} \cdot \mathrm{FSR}/V$, where L, V respectively denote the length and volume of the cavity. For a cavity field oscillating at $\omega \sim 10^{15}$ Hz for GaAs at 1064 nm ($\beta_{\mathrm{TPA}} = 260$ m/TW), we find $\alpha_{\mathrm{TPA}} \sim 10^{-8} \cdot \mathrm{FSR}$ for $L \approx 1$ mm, $V \approx 10^{-16}$ m^3. For typical intracavity photon numbers, the TPA contribution to the loss is then $10^{-2} \cdot \mathrm{FSR}$, a weak nonlinear background loss that is neglected for

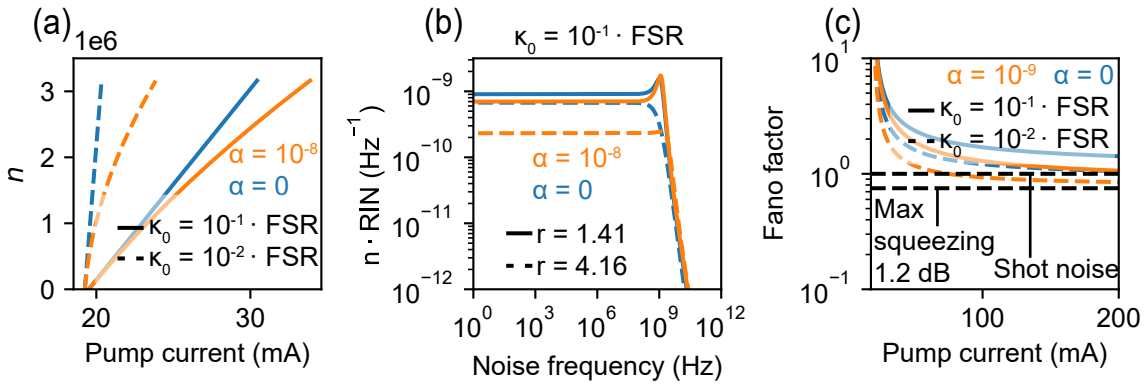

Figure A-2: **Steady state and noise plots for two photon absorption.** (a) Steady state intracavity photon number as a function of pump current (S-curve), demonstrating sub-linear dependence of photon number with pump current for two-photon absorption (TPA). (b) Photon number variance spectrum for two different pump powers $r = I/I_{\text{thres}}$, with broadband squeezing for intensity-dependent TPA. (c) Fano factor plots for linear and TPA loss profiles. The intensity dependence of TPA $\kappa(n) \propto n$ creates small (< 2 dB) drops in Fano factor below the shot noise limit when pumped far above threshold. Here, $\alpha \equiv \alpha_{\text{TPA}}/\text{FSR}$.

the examples in the main text where the primary nonlinear dispersive loss is much stronger.

As shown in Fig. A-2a, TPA creates a sublinear S-curve that arises from the monotonic dependence of $\kappa(n)$ on n. Fig. A-2b demonstrates how TPA induces broadband intensity noise squeezing, resulting in a weak suppression of Fano factor (integrated over all noise frequencies) in Fig. A-2c. Linear loss asymptotes to unit Fano factor for large pump powers, while TPA can result in minor noise condensation (though this effect can be washed out if TPA is too strong or too weak, in violation of $\kappa_0/n \ll \alpha_{\text{TPA}} \ll G_N$). The source of Fano factor reduction for higher pump currents is slightly different for both loss profiles. For linear loss, it occurs because steady state n increases linearly with pump current while the fluctuations $(\Delta n)^2$ have a sublinear dependence on pump current. In contrast, for TPA, the photon number n is clamped at high pump current and the photon number distribution is squeezed slightly due to the nonlinear loss $\kappa(n)$.

A.3.4 Noise reduction using nonlinear distributed feedback-based loss

In this section, we consider distributed feedback semiconductor lasers where a distributed Bragg reflector (DBR) is fabricated on one (or both) ends/facets of the laser cavity, or a VCSEL-type structure is employed. In this case, we use the analytical form for DBR reflectivity given by coupled mode theory [96, 97] to obtain

$$\kappa(\omega) = -\mathrm{FSR} \cdot \log \left| \frac{g \sinh(\theta)}{\Gamma \cosh(\theta) + (\alpha_{\mathrm{DBR}} + i\delta)\sinh(\theta)} \right|^2, \tag{A.26}$$

where $\beta = \omega\tilde{n}/c$ is the propagation constant (wavevector), $g = \omega\Delta n/(\pi c)$ is the approximate coupling coefficient, $\delta = \beta - \pi/d$, $\Gamma^2 = g^2 + (\alpha_{\mathrm{DBR}} + i\delta)^2$, $\theta = N_{\mathrm{DBR}} d\Gamma$, and α_{DBR} the radiative loss from the DBR. Here, N_{DBR} denotes the number of pairs of layers in the DBR, d the thickness of a pair of layers, Δn the index contrast, $\tilde{n}$ the effective index, and $\omega \equiv \omega(n, N)$ the laser frequency. Note that δ has the interpretation of a detuning from the Bragg value π/d (the center of the Bragg stop-band of maximum reflectivity and thus lowest loss is at $\delta = 0$). We would like to operate in the "sharp loss" regime, which is where the stop-band switches over to a pass-band, first occurring when $\theta = \pi \implies \delta^2 - g^2 = \pi^2/L^2$. For a lossless DBR, choosing the frequency ω_c at which this sharp transition occurs fixes δ and therefore Δn from the above relations:

$$\Delta n = \frac{\pi c}{\omega_c} \sqrt{\left(\frac{\tilde{n}}{c}(\omega_c - \omega_t)\right)^2 - \left(\frac{\pi}{L}\right)^2}, \tag{A.27}$$

where ω_t denotes the center of the stop band, so that $\omega_c - \omega_t$ is effectively the half-width of the stop band. The coupling coefficient g, index contrast Δn and stop band width $2(\omega_t - \omega_c)$ are thus closely related.

To use Eq. A.26, it is necessary to ensure the time response of the DBR is much faster than the free spectral range. We extract this time response by performing an FFT of $R(\omega)$. For lossy DBRs, $R(\omega)$ approaches a Lorentzian with width governed by α_{DBR}, and the maximum reflectivity may be far from unity. When the DBR is

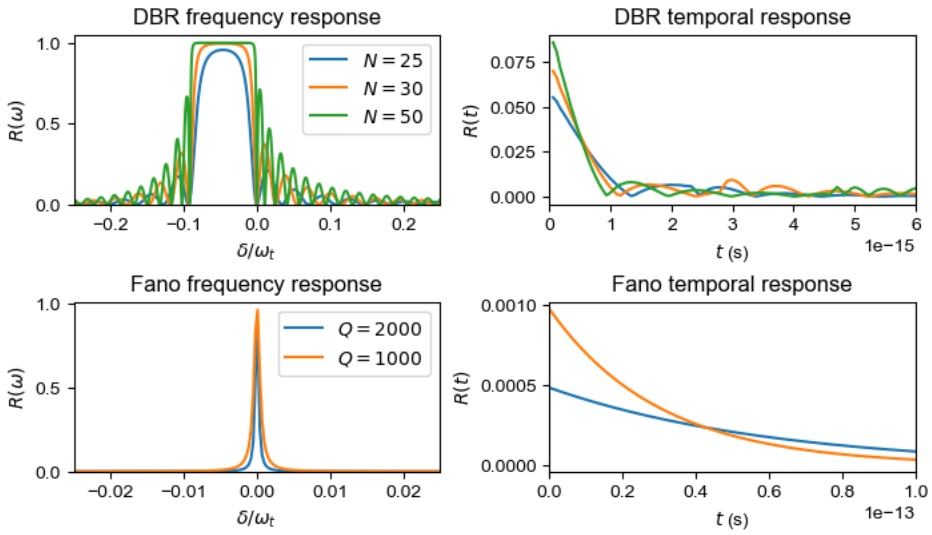

Figure A-3: **Comparison of frequency and temporal response for Fano mirror and DBR losses.** In the top row, the DBR stop band is made sharper and its width is increased by increasing the number of layers. This results in a shorter, ultrafast relaxation time. In contrast, in the bottom row, the Fano mirror frequency response is made sharper by increasing the quality factor (Q) of the resonance, which has the effect of decreasing the width of the resonance while increasing its lifetime.

lossless, an analytical expression for the time response is in general difficult to obtain. We observe that the time response is faster for DBRs of larger bandgap (wider stop bands). Intuitively, outcoupling in a lossless DBR is through the coupling coefficient g which scales with the index contrast Δn and thus correspondingly with the stop band width $2(\omega_c - \omega_t)$. This is distinct from the Fano resonances considered in the main text where the loss profile was derived from interference between a "direct channel" pathway bypassing the Fano resonance and an "indirect pathway" coupling to an intrinsic resonant mode of the photonic crystal. In such a case, the time response of the effective nonlinear dispersive loss is governed by the the complex resonance frequency of the Fano resonance (intuitively, how long light spends trapped in the photonic crystal). Here, however, sharply frequency-dependent loss arises from a different mechanism, namely the photonic bandgap of the DBR. A comparison of the two different types of temporal responses are provided in Fig. A-3.

The sharpness of $\kappa(n)$ increases with the number of layers N_{DBR} and Kerr nonlinear strength (the former corresponds to sharper evanescent decay of modes in the

photonic bandgap). For the strongest nonlinearity and sharpest $R(\omega)$, multiple stop bands may be accessible, corresponding to multiple regions of noise condensation and bistability for each transition from pass band to stop band. An important distinction from the Fano resonances considered earlier is that the sharp loss regions $\kappa_n > 0$ are now the lower bistability branches, accessible by simply pumping smoothly from threshold.

From an experimental standpoint, the sharpest loss (and strongest squeezing) can be obtained by maximizing the stop band width and number of layer pairs N_{DBR}. The former is limited by the intracavity saturation intensity and required index contrast Δn, while the latter is limited by fabrication methods. Nevertheless, carefully-engineered DBR-based losses when coupled to strong Kerr nonlinearity in semiconductor lasers may result in unprecedented broadband intensity noise squeezing.

A.4 Output photon noise

Here, we develop formalism to compute output photon noise in the presence of nonlinearity and dispersive dissipation. Let a, d respectively denote the nonlinear cavity mode and the Fano mirror mode, both of which couple to a continuum of far-field modes s_k (here k labels momentum). From the full Hamiltonian of the system [33], the Heisenberg equations of motion can be derived as

$$\begin{aligned}
\dot{a} &= -i\omega_a(1+\beta a^\dagger a)a + G(N)(1-i\alpha_L)a - i\sum_k g_k^* s_k + F_G \\
\dot{d} &= -i\omega_d d - i\sum_k v_k^* s_k \\
\dot{s}_k &= -i\omega_k s_k - i(g_k a + v_k d).
\end{aligned} \tag{A.28}$$

where $\omega_{a,d}$ denote the resonance frequencies of the cavity and Fano mirror, β is the per-photon Kerr nonlinearity, $G(N)$ is the carrier-dependent gain (added phenomenologically), α_L is the linewidth enhancement factor, and g_k, v_k are the couplings of a, d to the far-field mode s_k. $F_G(t)$ is a Langevin force term for the gain. We neglect direct coupling between a and d, though this can be readily incorporated into the

Heisenberg equations. We can solve for s_k as

$$s_k(t) = s_k(0)e^{-i\omega_k t} - i\int^t dt' e^{-i\omega_k(t-t')}[g_k a(t') + v_k d(t')]. \tag{A.29}$$

We assume momentum independent coupling $g = g_k, v = v_k$ and introduce $\kappa_{\rm FSR} = \pi\rho|g|^2, \gamma = \pi\rho|v|^2$. The input-output relation can then be found by taking $t \to \infty$, performing an integral over k, and Fourier transforming:

$$s_{\rm out}(\omega) = -s_{\rm in}(\omega) + \sqrt{2\kappa_{\rm FSR}}a(\omega) + \sqrt{2\gamma}d(\omega). \tag{A.30}$$

We can write the Fourier transformed Heisenberg equations for a, d as

$$\begin{aligned} -i\omega a &= -i\omega_a(1+\beta a^\dagger a)a + [G(N)(1-i\alpha_L) - \kappa_{\rm FSR}]a - \sqrt{\kappa_{\rm FSR}\gamma}d + \sqrt{2\kappa_{\rm FSR}}s_{\rm in} + F_G \\ -i\omega d &= -i\omega_d d - \gamma d - \sqrt{\kappa_{\rm FSR}\gamma}a + \sqrt{2\gamma}s_{\rm in}. \end{aligned} \tag{A.31}$$

Eliminating $d(\omega)$ as

$$d(\omega) = \frac{\sqrt{2\gamma}s_{\rm in} - \sqrt{\kappa_{\rm FSR}\gamma}a}{i\delta_d + \gamma}, \tag{A.32}$$

with $\delta_d \equiv \omega_d - \omega$, we can write the Fourier transformed equation of motion for a and the input-output relation as

$$-i\omega a = -i\omega_a(1+\beta a^\dagger a)a + [G(N)(1-i\alpha_L) - K_l(\omega)]a + \overbrace{K_c(\omega)s_{\rm in} + F_G}^{F_a} \tag{A.33}$$

$$s_{\rm out}(\omega) = K_a(\omega)a(\omega) - K_s(\omega)s_{\rm in}(\omega), \tag{A.34}$$

where

$$\begin{aligned} K_a(\omega) &= \sqrt{2\kappa_{\mathrm{FSR}}}\left(1-\frac{\gamma}{i\delta_d+\gamma}\right) \\ K_s(\omega) &= 1-\frac{2\gamma}{i\delta_d+\gamma} \\ K_l(\omega) &= \kappa_{\mathrm{FSR}}\left(1-\frac{\gamma}{i\delta_d+\gamma}\right) \\ K_c(\omega) &= K_a(\omega). \end{aligned} \tag{A.35}$$

To compute noise, we begin with the intracavity fluctuations, which are governed by the linearized system

$$M(\Omega)\begin{bmatrix}\delta a(\Omega)\\ \delta a^\dagger(\Omega)\\ \delta N(\Omega)\end{bmatrix} = \begin{bmatrix}F_a(\Omega)\\ F_{a^\dagger}(\Omega)\\ F_N(\Omega)\end{bmatrix} = \begin{bmatrix}K_c(\omega_+)\delta s_{\mathrm{in}}(\Omega)+F_G(\Omega)\\ K_c^*(\omega_-)\delta s_{\mathrm{in}}^\dagger(\Omega)+F_G^\dagger(\Omega)\\ F_N(\Omega)\end{bmatrix}, \tag{A.36}$$

where for a generic operator $X^\dagger(\Omega) = [X(-\Omega)]^\dagger$ follows from the definition $X^\dagger(t) = [X(t)]^\dagger$. The fluctuation matrix has columns

$$\begin{aligned} M_{x1}(\Omega) &= \begin{bmatrix}-i\omega_+ + i\omega_a(1+2\beta|\alpha|^2)+K_l(\omega_+)-G(N)(1-i\alpha_L)\\ -i\omega_a\beta\alpha^{*2}\\ 2G(N)\alpha^*\end{bmatrix} \\ M_{x2}(\Omega) &= \begin{bmatrix}i\omega_a\beta\alpha^2\\ i\omega_- - i\omega_a(1+2\beta|\alpha|^2)+K_l^*(\omega_-)-G(N)(1+i\alpha_L)\\ 2G(N)\alpha\end{bmatrix} \\ M_{x3}(\Omega) &= \begin{bmatrix}-G_N\alpha(1-i\alpha_L)\\ -G_N\alpha(1+i\alpha_L)\\ -i\omega+\gamma_\parallel+2G_N|\alpha|^2\end{bmatrix}. \end{aligned} \tag{A.37}$$

Here, $x \in [1,2,3]$ to denote the row of M, $\omega_\pm = \omega \pm \Omega$, and the steady state cavity amplitude α is determined through

$$[i(-\omega_a(1+\beta|\alpha|^2)+\omega)+G(N)(1-i\alpha_L)-K_l(\omega)]\alpha = 0. \tag{A.38}$$

Noise emerges from the nonzero correlators [2, 98]

$$\begin{aligned}
\langle F_G^\dagger(\omega) F_G(\omega')\rangle &= G(N)\delta(\omega-\omega') \\
\langle F_N^\dagger(\omega) F_G(\omega')\rangle &= -\alpha G(N)\delta(\omega-\omega') \\
\langle F_N^\dagger(\omega) F_N(\omega')\rangle &= [nG(N)+\gamma_\parallel N+\epsilon I]\delta(\omega-\omega') \\
\langle s_{\rm in}(\omega) s_{\rm in}^\dagger(\omega')\rangle &= \delta(\omega-\omega'),
\end{aligned} \tag{A.39}$$

with $\epsilon = 0$ for quiet pumping and $\epsilon = 1$ for shot noise limited pumping. We can now compute the output photon noise by noting

$$\begin{aligned}
\delta n_{\rm out}(t) &= s_0^*\delta s_{\rm out}(t) + s_0\delta s_{\rm out}^\dagger(t) \\
\delta n_{\rm out}(\Omega) &= s_0^*\delta s_{\rm out}(\Omega) + s_0[\delta s_{\rm out}(-\Omega)]^\dagger \\
&= s_0^* K_a(\omega_+)\delta a(\Omega) + s_0 K_a^*(\omega_-)\delta a^\dagger(\Omega) - [s_0^* K_s(\omega_+)\delta s_{\rm in}(\Omega) + s_0 K_s^*(\omega_-)\delta s_{\rm in}^\dagger(\Omega)]
\end{aligned} \tag{A.40}$$

where here $s_0(\omega) = K_a(\omega)\alpha(\omega)$ is the steady state output (propagating) amplitude and the intensity noise spectrum is given by $\langle \delta n_{\rm out}^\dagger(\Omega)\delta n_{\rm out}(\Omega)\rangle$. Spectra in the limit of nondispersive loss closely match those found by Yamamoto et al. [98].

A.5 Intensity noise in QCLs with nonlinear dispersive loss

The photon and carrier dynamics for QCLs are conventionally described using a three-level model for the carrier populations [3]

$$\begin{aligned}
\dot N_3^j &= I^j - N_3^j\left(\frac{1}{\tau_{32}}+\frac{1}{\tau_{31}}\right) - nG\left(N_3^j, N_2^j\right) + F_3^j \\
\dot N_2^j &= \frac{N_3^j}{\tau_{32}} - \frac{N_2^j}{\tau_{21}} + nG\left(N_3^j, N_2^j\right) + F_2^j \\
\dot n &= n\left(-\kappa(n) + \sum_{j=1}^{m} G\left(N_3^j, N_2^j\right)\right) + F_n,
\end{aligned} \tag{A.41}$$

where N_3^j, N_2^j respectively denote the carrier populations in levels 3 and 2 in each gain stage j, I^j denotes the injected current to gain stage j, and $\tau_{31}, \tau_{32}, \tau_{21}$ are the nonradiative decay time constants indicated in Fig. 4c. A linear model for the gain $G\left(N_3^j, N_2^j\right) = G_N(N_3^j - N_2^j)$ is employed. Langevin forces F_n^j, F_3^j, F_2^j are added for the following noise analysis.

We can simplify the analysis by introducing $N_{2,3} = \sum_j N_{3,2}^j$ and assuming all of the gain stages are identical. Then, the dynamics for n, N_2, N_3 are described by a set of three coupled nonlinear equations. Note that we neglect the dynamics of N_1 (the carrier population in level 1) since the populations of interest n, N_2, N_3 form a closed system of equations. Linearizing and Fourier transforming the QCL rate equations, we find

$$M \begin{bmatrix} \delta N_3(\Omega) \\ \delta N_2(\Omega) \\ \delta n(\Omega) \end{bmatrix} = \begin{bmatrix} F_3 \\ F_2 \\ F_n - n\kappa_\omega F_\phi \end{bmatrix}$$

with the fluctuation matrix

$$M = \begin{bmatrix} -i\Omega + \gamma_{11} & -\gamma_{12} & \gamma_{13} \\ -\gamma_{21} & -i\Omega + \gamma_{22} & -\gamma_{23} \\ -\gamma_{31} & \gamma_{32} & -i\Omega - \gamma_{33} \end{bmatrix},$$

where $\gamma_{11} = nG_N + 1/\tau_{32} + 1/\tau_{31}, \gamma_{12} = nG_N, \gamma_{13} = \gamma_{23} = G_N\Delta N, \gamma_{21} = nG_N + 1/\tau_{32}, \gamma_{22} = nG_N + 1/\tau_{21}, \gamma_{31} = \gamma_{32} = nG_N, \gamma_{33} = -n\kappa_n$ and $\Delta N = N_3 - N_2$. The correlators between the Langevin forces are given by $\langle 2D_{nn}\rangle = 2G_N N_3 n$, $\langle 2D_{\phi\phi}\rangle = G_N N_3/(2n)$, $\langle 2D_{22}\rangle = 2G_N N_3 n + N_3/\tau_{32}$, $\langle 2D_{33}\rangle = 2G_N N_3 n + N_3/\tau_{32} + N_3/\tau_{31}$, $\langle 2D_{3n}\rangle = -G_N\left(N_2 + N_3\right)n$, $\langle 2D_{2n}\rangle = G_N\left(N_2 + N_3\right)n$, $\langle 2D_{32}\rangle = -\left(G_N(N_2 + N_3)n + N_3/\tau_{32}\right)$.

In QCLs, the intensity noise is dominated by both spontaneous emission and nonradiative decay of excited carriers, whereas in typical semiconductor lasers, it is only the former that matters [99]. Thus, starting from the linearized matrix equations,

we can approximate the DC intensity noise as

$$\langle \delta n^\dagger(0)\delta n(0)\rangle \approx \frac{\gamma_s^2(\gamma_{21}-\gamma_{22})^2\langle 2D_{33}\rangle + (\gamma_s\gamma_{21}-\gamma_{11}\gamma_{22})^2\langle 2D_{nn}\rangle}{\left(\gamma_s^2\gamma_{23}+\gamma_{11}\gamma_{22}\gamma_{33}+\gamma_s(\gamma_{13}(\gamma_{21}-\gamma_{22})-\gamma_{11}\gamma_{23}=\gamma_{21}\gamma_{33})\right)^2}, \quad \text{(A.42)}$$

where $\gamma_s = \gamma_{12} = \gamma_{31} = \gamma_{32} = nG_N$. In the absence of nonlinear dispersive loss, $\gamma_{33} = 0$ and the DC intensity noise goes as $(\tau_s/\tau_{\rm nr})^2$ where $1/\tau_s \equiv nG_N$ is the rate of stimulated emission (per carrier) and $1/\tau_{\rm nr}$ is an effective nonradiative decay rate of the carriers. The scaling with the stimulated emission lifetime is expected given that the light approaches a coherent state as the power increases. The inverse scaling with $\tau_{\rm nr}$ reflects the fact that in QCLs, in contrast to conventional semiconductor lasers, the carrier density is not clamped above threshold. Instead, N_2, N_3 are dynamic and their fluctuations have fast response times, significantly affecting the intensity noise even above threshold. We also note that the fast nonradiative decay of the carriers also leads to the relaxation oscillations in QCLs being overdamped, despite increasing intensity noise. In this case, the increased intensity noise of QCLs compared to conventional lasers stems from stronger low-frequency noise arising from the unclamped carrier populations above threshold (which increase proportionately with pump current, together with the photon number). The effect of nonlinear dispersive loss is to outcompete the nonradiative decay rates to dominate the intensity noise. Thus, $|\gamma_{33}| \gg 1/\tau_{\rm nr}$ is a necessary condition for this mechanism for squeezing to be effective.

To provide analytical checks against previous theory on QCL intensity noise [3], we compute output photon noise as described above in Sec. A.4, agreeing qualitatively with Eq. 95 of [3].

A.6 Nonlinear dispersive loss with carrier and Kerr nonlinearities

In this section, we describe how the interplay of carrier nonlinearity with dispersive loss can result in unexplored "carrier bistability" behavior in conventional semiconductor lasers. We consider carrier nonlinear strengths σ comparable to what they

might be in, for example, GaAs-based gain media [32, 95].

We first describe how multiple lasing steady states can exist when strong carrier nonlinearity and dispersive loss are simultaneously present. In an ordinary semiconductor laser, the "gain equals loss" requirement leads to a so-called "gain clamping" condition, wherein above threshold, the inverted carrier density is fixed at some value, regardless of the intensity (i.e. the carrier density N such that $G_N(N - N_{\text{trans}}) = \kappa$). This is depicted in Fig. A-4a by the "linear loss" case which shows only a single intersection point of the carrier-dependent gain and carrier-independent loss. However, in the presence of strong carrier nonlinearity and sharply frequency-dependent outcoupling (with a Fano mirror for example), the loss of the cavity mode can depend nonlinearly on the carrier density N, $\kappa(\omega(N)) = \kappa(N)$. As the carrier density changes, so does the cavity frequency, and hence the damping rate via the frequency-dependent mirror. The "gain equals loss" condition now reads $G_N(N-N_{\text{trans}}) = \kappa(N)$. As shown in Fig. A-4a, this leads to a situation where more than one carrier density N can cause gain and loss to be equal, corresponding to multiple cavity resonance frequencies. In the case of the Fano resonance, we see that up to three different steady states are possible.

Fig. A-4b shows how this phenomenon manifests in the steady state laser behavior. The dependence of steady state intensity on the pump current is still linear, but there can be up to three independent branches, corresponding to different steady state N and different lasing frequencies. For the Fano mirror example, one resonance frequency is always present such that the detuning from the Fano resonance $\Delta \approx 0$. Since this solution has lowest loss, and thus the lowest threshold, lasing will occur here by default. The other branches are also stable, but disconnected from the lowest branch. It may be possible to experimentally access these higher branches through dynamic pumping schemes which generate transients that can travel from one branch to another.

When Kerr nonlinearity is also introduced, additional phenomena appear due to the simultaneous nonlinear dependence of the damping rate on intensity and carrier number. It is important to note that the profile $\kappa(\omega)$ is unchanged, though $\kappa(n, N)$

will vary based on the nonlinear strengths. Furthermore, the gain (and thus loss) is monotonically increasing in N. For typical materials (and for the results presented in Fig. A-4), $\sigma < 0$ increases the resonance frequency $\omega_R(n, N)$ and thus pushes lasing solutions rightward along $\kappa(\omega)$.

Consider first weak carrier nonlinearity (orange and green curves in Fig. A-4c). Then, the carrier nonlinearity can be treated as a perturbation to the initially symmetric Lorentzian loss $\kappa(n)$. On the $\kappa_\omega \equiv d\kappa/d\omega > 0$ (right) branch of the dispersive loss, the carrier nonlinearity shifts the loss curve upward. On the other hand, the $\kappa_\omega < 0$ (left) branch shifts downwards since an increase in ω corresponds to a point of lower loss (approaching detuning $\Delta = 0$).

Suppose we increase the carrier nonlinearity further (red curve in Fig. A-4c). For n near threshold, far below the "magic" photon number $n_c \approx 10^6$ of lowest loss, the carrier nonlinearity pushes solutions rightward along the Lorentzian. However, the laser still lies on the $\kappa_\omega < 0$ branch - the carrier nonlinearity pushes the mode closer to n_c, which is near zero loss and thus $N \approx N_{\text{trans}}$. This yields one steady state solution. For higher n, near but still below n_c, we eventually reach an n at which two solutions are possible: $N \approx N_{\text{trans}}$ (lower loss) or $N > N_{\text{trans}}$ (higher loss). Immediately afterwards, a third solution is possible with still higher loss/higher carrier density, phenomenologically similar to the dashed curve in Fig. A-4a. Finally, as κ_ω drops past the inflection point of $\kappa(\omega)$, a point corresponding to two solutions marks the end of the carrier bistability and for the largest n we again obtain only one solution (the Lorentzian loss looks approximately linear).

For even stronger carrier nonlinearity (purple curve in Fig. A-4c), the carrier bistability boundaries shift leftward in photon number. Comparing the red and purple curves in Fig. A-4c, the left boundary eventually crosses zero and becomes negative, at which point the loss curve detaches into two parts: a sharp part at low loss and linear part at higher loss, separated by a range of pump currents over which no stable lasing solution occurs. When the right bistability boundary also crosses $n = 0$ the sharp loss vanishes and laser operation only occurs on the linear high-loss branch (with correspondingly larger threshold currents), as shown for the brown curve in

Fig. A-4c.

We now examine the effects of this carrier bistability on intensity noise. As shown in Fig. A-4e, the minimum achievable Fano factor is relatively independent of the level of carrier nonlinearity. This can be seen by noting that the first term in Eq. A.24 dominates the Fano factor at these points. However, past the sharp loss region, the linear branch created by the carrier nonlinearity possesses a higher loss that pulls the Fano factor upward for larger pump currents. For large carrier nonlinearities, the system eventually hits bistability and a region of unstable lasing, transitioning to (approximately) linear behavior again. For carrier nonlinearities much stronger than the Kerr nonlinearity (brown curve), approximately linear loss is restored as described above and no intensity noise reduction is observed. Mathematically, Eq. A.24 essentially contains a combination of dominant Kerr and dominant carrier nonlinearity terms, demarcated by pump currents smaller and larger than the Fano factor minimum/sharp loss regime, respectively.

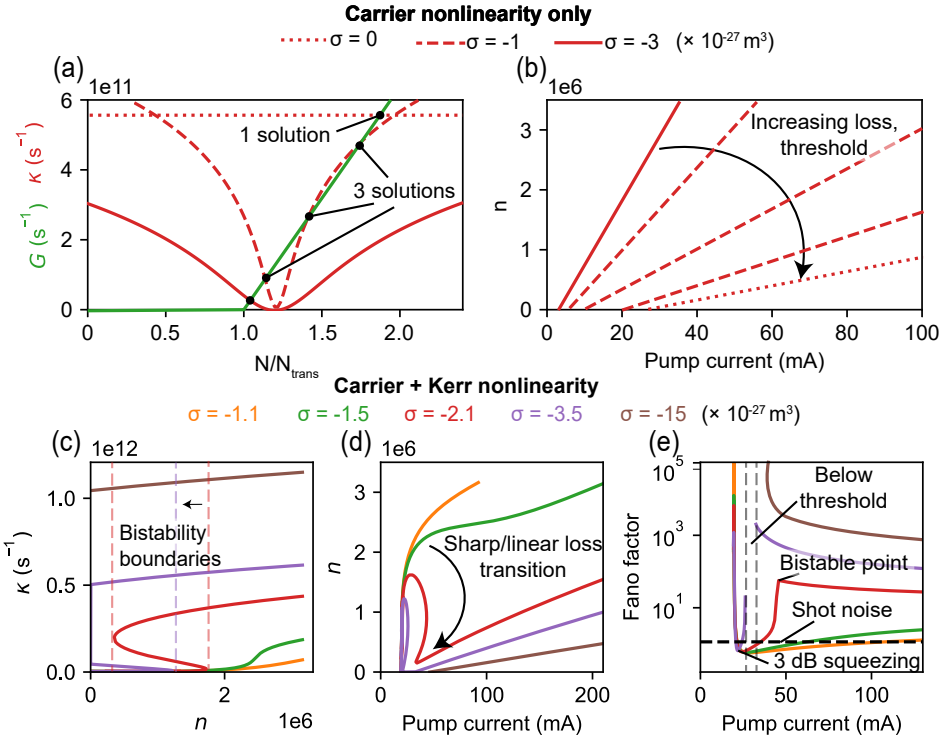

Figure A-4: **Effects of carrier and Kerr nonlinearities composed with dispersive loss**. (a) In the presence of only carrier nonlinearity σ, the resonance frequency and thus loss depend "directly" on carrier density N, and steady states are set by the intersections of gain and loss. For strong σ and low background loss κ_0, multiple steady state carrier densities N can correspond to a given photon number n, resulting in different steady state losses (detunings from the Fano resonance). The lowest loss solution (smallest detuning) is most likely to lase, though extra solutions may be accessible by dynamic pumping schemes. (b) The schematic effect of this "carrier bistability" is to create multiple branches in the S-curve of different slope/threshold current. The presence of both strong carrier and Kerr nonlinearities result in the novel behaviors shown in panels (c), (d), and (e). Carrier nonlinearity causes a deformation of the intensity-nonlinear Lorentzian loss profile, eventually pinching off the "sharp loss" from the linear loss for sufficiently strong carrier nonlinearity (purple curve). This stems from leftward motion of the carrier bistability boundaries and creates a demarcation between linear ($F \gg 1$) and nonlinear ($F < 1$) loss regimes which may be separated by a region of lasing with no stable solution. System parameters used are the same as those in Fig. 2 with $\beta = -10^{-10}$, $\kappa_0 = 10^{-2} \cdot \mathrm{FSR}$, and $\gamma = 2 \times 10^{12}$ rad/s. The magnitudes of Kerr and carrier nonlinearities taken here are comparable to what they might be in GaAs-based gain media: $\beta \sim -10^{-10}$ and $\sigma \sim -3 \times 10^{-27}$ m^3 (with the proviso of being taken as instantaneous and being evaluated at a single wavelength).

Appendix B

Appendix for multimode amplitude squeezing through cascaded nonlinear optical processes

B.1 Heisenberg-Langevin equations and noise analysis

The equations of motion provided in the main text are obtained by finding the Heisenberg-Langevin equations for the Hamiltonian

$$H/\hbar = \sum_n \omega_n a_n^\dagger a_n + i\kappa \sum_n \left(a_T^\dagger a_n^\dagger a_{n-1} - \text{h.c.} \right), \tag{B.1}$$

and supplementing decay terms and their corresponding Langevin forces. The result, including intrinsic losses and working in the interaction picture, is

$$\begin{aligned} \dot{a}_T &= \kappa \sum_n a_n^\dagger a_{n-1} - (\gamma_T + \mu_T) a_T + \sqrt{2\gamma_T} s_T + \sqrt{2\mu_T} f_T \\ \dot{a}_n &= \kappa \left(a_T^\dagger a_{n-1} - a_{n+1} a_T \right) - (\gamma_n + \mu_n) a_n + \sqrt{2\gamma_n} s_n + \sqrt{2\mu_n} f_n, \end{aligned} \tag{B.2}$$

where $\langle s_{0,1} \rangle \neq 0$ since these two modes are pumped (initial pump and seed, respectively), $f_n, s_{n\neq 0,1}$ are zero mean Langevin forces that satisfy the conventional correlator $\langle f_n(t) f_n^\dagger(t') \rangle = \delta(t - t')$ and likewise for s_n (s_n, f_n do not couple to each other since they are distinct decay channels). These correlators can be derived rigorously by considering the complete Hamiltonian with coupling to the bath of all vacuum modes (or, more precisely, thermal states, but we assume the thermal occupation $n_{\text{th}} \ll 1$, which is true under most experimental conditions). For example, the Langevin forces s_n give rise to amplitude noise due to outcoupling to far-field vacuum modes. The Langevin force associated with this process for the quadrature $p_n = a_n + a_n^\dagger$ in Eq. 3.2 is given by

$$F_n = \sqrt{2\gamma_n}(\delta s_n + \delta s_n^\dagger) \tag{B.3}$$

In computing the amplitude noise $\langle \delta p_n^\dagger \delta p_n \rangle$, the Langevin force correlator is then

$$\langle F_n^\dagger F_n \rangle / 2\gamma_n = \langle \delta s_n^2 + \delta s_n^{\dagger 2} + 2\delta s_n^\dagger \delta s_n + 1 \rangle \tag{B.4}$$

$$= -\langle s_n \rangle^2 + \langle s_n^2 \rangle - \langle s_n^\dagger \rangle^2 + \langle s_n^{\dagger 2} \rangle + 2[\langle s_n^\dagger s_n \rangle - \langle s_n^\dagger \rangle \langle s_n \rangle] + 1 \tag{B.5}$$

where s_n is an annihilation operator for the external mode of frequency ω_n satisfying the commutator $[s_n, s_n^\dagger] = 1$. If the external mode is either vacuum or a coherent state, the above expression reduces to 1.

The steady state solutions to the Heisenberg-Langevin equations can be found by setting $\dot{a}_n = \dot{a}_T = 0$ and using the mean values for the incoupled fields (zero except for modes that are externally pumped). This results in a system of nonlinear coupled equations that can be solved numerically given the initial modal amplitude distribution. To compute noise spectra, we perform a linearization about the mean field such that $M(\omega)P(\omega) = F(\omega)$, where $P(\omega) = [\delta p_0(\omega) \delta p_1(\omega) \cdots \delta p_N(\omega) \delta p_T(\omega)]^T$ and $F(\omega) = [F_0(\omega) F_1(\omega) \cdots F_N(\omega) F_T(\omega)]^T$ with the fluctuation matrix (shown here

for a system with modes a_T and $a_{0,1,\ldots,N}$) given by

$$M(\omega) = \begin{bmatrix} -i\omega+\gamma_0 & \kappa a_T & \ldots & \ldots & \ldots & \kappa a_1 \\ -\kappa a_T & -i\omega+\gamma_1 & \kappa a_T & \ldots & \ldots & \kappa(a_2-a_0) \\ \vdots & \vdots & \vdots & \vdots & \vdots & \vdots \\ -\kappa a_1 & -\kappa(a_0+a_2) & \ldots & -\kappa(a_{N-2}+a_N) & -\kappa a_{N-1} & -i\omega+\gamma_T \end{bmatrix}.$$

A useful metric to quantify the quantum nature of squeezed light is the photon number (intensity) noise $\langle \delta n^\dagger \delta n \rangle$, where $n = a^\dagger a$ denotes the photon number operator. We can show using the mean field approximation $a = \alpha + \delta a$ (with α a complex number and δa an operator) that

$$\begin{aligned} \langle \delta n^\dagger \delta n \rangle &= \left\langle \left(\alpha^* \delta a + \alpha \delta a^\dagger\right)\left(\alpha \delta a^\dagger + \alpha^* \delta a\right) \right\rangle \\ &= |\alpha|^2 \left\langle \delta a \delta a^\dagger + \delta a^\dagger \delta a \right\rangle \\ &= |\alpha|^2 \langle \delta p^\dagger \delta p \rangle, \end{aligned} \tag{B.6}$$

where $\langle n \rangle = |\alpha|^2$ and $p = a + a^\dagger$. Thus, the intensity noise spectrum relative to the shot noise limit $F(\omega) = \Delta n^2(\omega)/\langle n \rangle$ is directly given by $\langle \delta p^\dagger(\omega) \delta p(\omega) \rangle$. In the case of intracavity statistics, we can integrate over frequency to get the total Fano factor, defined as $F = \Delta n^2 / \langle n \rangle$:

$$F = \int \frac{d\omega}{2\pi} \langle \delta p^\dagger(\omega) \delta p(\omega) \rangle. \tag{B.7}$$

Note that $F < 1$ indicates sub-Poissonian statistics and quantum mechanically-squeezed light. For the cases presented in the main text, we have found no significant squeezing in F due to the presence of relaxation oscillations from the strong nonlinear processes inside the cavity. However, in the case of a single TWM process, we have verified the established 3 dB squeezing limit in F for the signal and idler modes [9].

B.1.1 Quantum noise of coherently driven state with dissipation

The Heisenberg-Langevin equation for a single mode evolving under driven-dissipative dynamics (alone) reads

$$\dot{a}_n = -\gamma_n a_n + \sqrt{2\gamma_n} s_n \tag{B.8}$$

On linearizing and Fourier transforming about the steady state, we obtain

$$\delta a_n(\omega) = \frac{\sqrt{2\gamma_n}\delta s_n(\omega)}{-i\omega + \gamma_n}, \tag{B.9}$$

which for a coherent pump gives the intracavity amplitude noise spectrum

$$\langle \delta p^\dagger_{n,\mathrm{in}}(\omega)\delta p_{n,\mathrm{in}}(\omega)\rangle = \frac{2\gamma_n}{\omega^2+\gamma_n^2}. \tag{B.10}$$

It is straightforward to show that $\int_0^\infty \frac{d\omega}{\pi}\langle \delta p^\dagger_{n,\mathrm{in}}(\omega)\delta p_{n,\mathrm{in}}(\omega)\rangle = 1$, as expected for a coherent state. The output fluctuations can be computed similarly for the output propagating field $a_{n,\mathrm{out}} = -s_n + \sqrt{2\gamma_n}a_{n,\mathrm{in}}$ which yields

$$\begin{aligned}
\langle \delta p^\dagger_{n,\mathrm{out}}(\omega)\delta p_{n,\mathrm{out}}(\omega)\rangle &= 1 + 2\gamma_n\langle \delta p^\dagger_{n,\mathrm{in}}(\omega)\delta p_{n,\mathrm{in}}(\omega)\rangle - 2\mathrm{Re}\left(\delta s_n(\omega)\delta a^\dagger_{n,\mathrm{in}}(\omega)\right) \\
&= 1 + \frac{4\gamma_n^2}{\omega^2+\gamma_n^2} - \frac{4\gamma_n^2}{\omega^2+\gamma_n^2} \\
&= 1.
\end{aligned} \tag{B.11}$$

B.2 Estimation of nonlinear strength

In this section, we provide a rough estimation of typical nonlinear strengths κ in a free space multimode cavity. As derived from first-order perturbation theory [72],

$$\kappa = 2d_{\mathrm{eff}}\sqrt{\frac{\hbar\omega_T\omega_1\omega_2}{\epsilon_0}}\frac{\int_{\mathrm{NL}} dV E_1E_2E_T}{\sqrt{\int_{\mathrm{cav}} dV\epsilon_{1r}|E_1|^2}\sqrt{\int_{\mathrm{cav}} dV\epsilon_{2r}|E_2|^2}\sqrt{\int_{\mathrm{cav}} dV\epsilon_{Tr}|E_T|^2}} \tag{B.12}$$

For concreteness, we consider GaAs, for which $d_{\text{eff}} = 274$ pm/V [**?**]. Then, with frequencies $\omega_1 = 2\pi \cdot 282$ THz, $\omega_2 = 2\pi \cdot 281$ THz, and $\omega_T = 2\pi \cdot 1$ THz, we have refractive indices $n_{1,2} = \sqrt{\epsilon_{1r,2r}} \approx 3.5$ and $n_T = \sqrt{\epsilon_{Tr}} \approx 3.0$. We assume the electric field profiles $E_{1,2,T}$ are uniform over a cross-section $A \approx 4 \times 10^{-6}$ m^2 and that the crystal length is $L_{\text{NL}} \approx 3$ mm while the cavity length is $L_{\text{cav}} \approx 50$ cm. Then, we have

$$\begin{aligned} \kappa &= \frac{2d_{\text{eff}}}{n_1 n_2 n_T} \sqrt{\frac{\hbar \omega_T \omega_1 \omega_2}{\epsilon_0}} \frac{AL_{\text{NL}}}{(AL_{\text{cav}})^{3/2}} \\ &\approx 3.32 \text{ s}^{-1}, \end{aligned} \tag{B.13}$$

closely matching the order of magnitude for values of κ considered in the main text.

B.3 Frequency comb generation

By carefully engineering the Q factor for different frequency modes in the multimode cavity, it is possible to create one-sided frequency combs (consisting exclusively of redshifted or blueshifted modes relative to the pump mode at ω_0) or two-sided frequency modes, as shown in Fig. B-1. The modes that comprise the frequency space cavity where nonlinear energy flow is strong have high Q factor. For example, in the redshifted comb, blueshifted modes are very leaky (low Q factor), are not part of the frequency space cavity, and do not get populated through nonlinear coupling. Notice that including blueshifted modes reduces the efficiency of generating the terahertz idler mode since terahertz photons are destroyed in upconversion processes that generate the blueshifted modes. Therefore, the first configuration in Fig. B-1 (which we consider in the main text) is optimal for maximizing generation of terahertz idler photons and thus the nonlinear rate in the cavity.

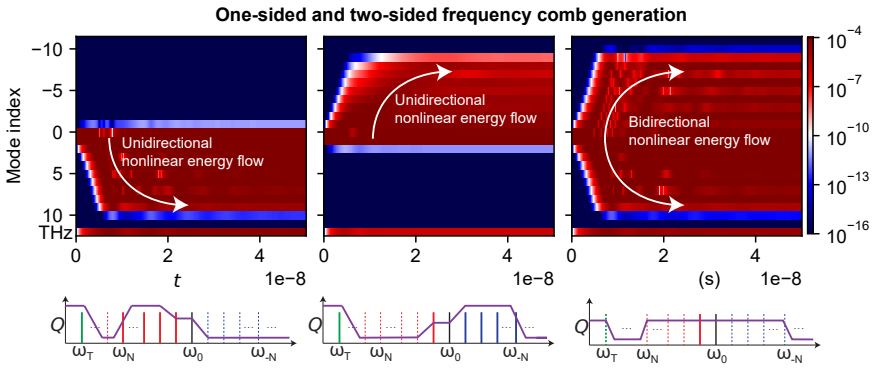

Figure B-1: **One-sided and two-sided frequency comb generation.** Q factor shaping (through the use of frequency-dependent couplers) permits the creation of frequency combs containing only redshifted or blueshifted (one-sided) or both redshifted and blueshifted (two-sided) modes relative to the pump.

B.4 Multimode correlation matrix

In this section, we plot and analyze the correlation matrix C of the multimode system, where the entries of C are computed according to

$$C_{ij} = \frac{\langle \delta p_i^\dagger \delta p_j \rangle}{\sqrt{\langle \delta p_i^\dagger \delta p_i \rangle \langle \delta p_j^\dagger \delta p_j \rangle}}. \tag{B.14}$$

Here, all noises (intracavity and output) are computed at zero Fourier frequency, so the following discussion only applies to low-frequency noise (up to around 100 MHz). In the presence of weak nonlinear coupling (Fig. B-2a,b) between modes, the correlation coefficient between the amplitude noise of different modes is dominated by simple driven-dissipative dynamics. The correlation coefficients are most sensitive for the high Q factor cascading orders. Almost all correlations are positive, indicating that, as expected, (outcoupling) loss of photons from one of these modes is correlated with loss in the signal and idler of the corresponding TWM/downconversion process (and vice versa for the upconversion). This is reflected in both the intracavity and output noise correlation coefficients. With strong nonlinearity, the correlation matrix is now significantly altered by the nonlinear dynamics. The interference from the counter-propagating Bloch waves is reflected in the checkerboard pattern of the intracavity correlation matrix, which results in alternating positive and negative cor-

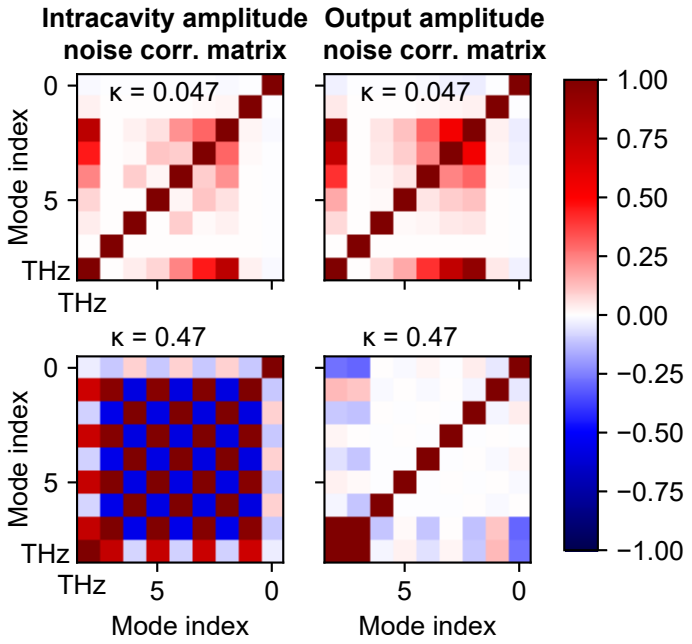

Figure B-2: **Correlation matrix showing interplay between nonlinear coupling and dissipation.** (a), (b) In the presence of weak nonlinearity, the correlations are driven by the dissipative dynamics. In particular, the correlations are most sensitive amongst the high Q factor cascading orders and the THz bath. All correlations are positive since loss in one of these modes reduces the conversion efficiency of another. (c), (d) In the presence of stronger nonlinearity, the correlation matrix heatmap changes noticeably. Correlations are now dominated by the nonlinear dynamics, where the effect of Bloch mode interference can be seen in the checkerboard pattern in the cascading orders. The output noise correlation matrix notably displays strong positive correlation between the THz bath mode and certain IR modes (here, the two frequency mirror modes $a_{0,N}$, likely because these two modes have the strongest outcoupling). In this simulation, $N = 7$ cascading orders are considered and the quality factors are $Q_r = 10^8, Q_b = 10^2, Q_0 = Q_N = 10^5, Q_T = 10^4$.

relation coefficients for modes within the frequency space cavity. Furthermore, the output correlation matrix shows evidence for strong, long-range correlations between the THz bath mode a_T and the leaky IR frequency mirror modes $a_{0,N}$.

Bibliography

[1] Yi Yu, Weiqi Xue, Elizaveta Semenova, Kresten Yvind, and Jesper Mork. Demonstration of a self-pulsing photonic crystal fano laser. *Nature Photonics*, 11(2):81–84, 2017.

[2] Weng W Chow, Stephan W Koch, and Murray III Sargent. *Semiconductor-laser physics*. Springer Science & Business Media, 2012.

[3] Farhan Rana and Rajeev J Ram. Current noise and photon noise in quantum cascade lasers. *Physical Review B*, 65(12):125313, 2002.

[4] Xing-Guang Wang, Frédéric Grillot, and Cheng Wang. Rate equation modeling of the frequency noise and the intrinsic spectral linewidth in quantum cascade lasers. *Optics Express*, 26(3):2325–2334, 2018.

[5] Sahil Pontula, Jamison Sloan, Nicholas Rivera, and Marin Soljacic. Strong intensity noise condensation using nonlinear dispersive loss in semiconductor lasers. *arXiv preprint arXiv:2212.07300*, 2022.

[6] Sahil Pontula. *Developing and Characterizing Sources of Quantum States of Light: from Single Photons to Million-Photon Fock States*. PhD thesis, Massachusetts Institute of Technology, 2023.

[7] Benjamin J Lawrie, Paul D Lett, Alberto M Marino, and Raphael C Pooser. Quantum sensing with squeezed light. *Acs Photonics*, 6(6):1307–1318, 2019.

[8] Lars S Madsen, Fabian Laudenbach, Mohsen Falamarzi Askarani, Fabien Rortais, Trevor Vincent, Jacob FF Bulmer, Filippo M Miatto, Leonhard Neuhaus,

Lukas G Helt, Matthew J Collins, et al. Quantum computational advantage with a programmable photonic processor. *Nature*, 606(7912):75–81, 2022.

[9] MJ Collett and CW Gardiner. Squeezing of intracavity and traveling-wave light fields produced in parametric amplification. *Physical Review A*, 30(3):1386, 1984.

[10] R Dassonneville, R Assouly, T Peronnin, AA Clerk, A Bienfait, and B Huard. Dissipative stabilization of squeezing beyond 3 db in a microwave mode. *PRX Quantum*, 2(2):020323, 2021.

[11] Wei Qin, Adam Miranowicz, and Franco Nori. Beating the 3 db limit for intracavity squeezing and its application to nondemolition qubit readout. *Physical Review Letters*, 129(12):123602, 2022.

[12] Ling-An Wu, HJ Kimble, JL Hall, and Huifa Wu. Generation of squeezed states by parametric down conversion. *Physical review letters*, 57(20):2520, 1986.

[13] Henning Vahlbruch, Moritz Mehmet, Simon Chelkowski, Boris Hage, Alexander Franzen, Nico Lastzka, Stefan Gossler, Karsten Danzmann, and Roman Schnabel. Observation of squeezed light with 10-db quantum-noise reduction. *Physical review letters*, 100(3):033602, 2008.

[14] Henning Vahlbruch, Moritz Mehmet, Karsten Danzmann, and Roman Schnabel. Detection of 15 db squeezed states of light and their application for the absolute calibration of photoelectric quantum efficiency. *Physical review letters*, 117(11):110801, 2016.

[15] ES Polzik, J Carri, and HJ Kimble. Spectroscopy with squeezed light. *Physical review letters*, 68(20):3020, 1992.

[16] MJ Collett and DF Walls. Quantum limits to light amplifiers. *Physical review letters*, 61(21):2442, 1988.

[17] Yoshihisa Yamamoto, Susumu Machida, and Wayne H Richardson. Photon number squeezed states in semiconductor lasers. *Science*, 255(5049):1219–1224, 1992.

[18] R Paschotta, M Collett, P Kürz, K Fiedler, HA Bachor, and J Mlynek. Bright squeezed light from a singly resonant frequency doubler. *Physical review letters*, 72(24):3807, 1994.

[19] S Schmitt, J Ficker, M Wolff, F König, A Sizmann, and Gerd Leuchs. Photon-number squeezed solitons from an asymmetric fiber-optic sagnac interferometer. *Physical review letters*, 81(12):2446, 1998.

[20] QA Turchette, N Ph Georgiades, CJ Hood, HJ Kimble, and AS Parkins. Squeezed excitation in cavity qed: Experiment and theory. *Physical Review A*, 58(5):4056, 1998.

[21] Margareta Wallquist, Klemens Hammerer, Peter Zoller, Claudiu Genes, Max Ludwig, Florian Marquardt, Philipp Treutlein, Jun Ye, and H Jeff Kimble. Single-atom cavity qed and optomicromechanics. *Physical Review A*, 81(2):023816, 2010.

[22] V Peano, HGL Schwefel, Ch Marquardt, and F Marquardt. Intracavity squeezing can enhance quantum-limited optomechanical position detection through deamplification. *Physical Review Letters*, 115(24):243603, 2015.

[23] Jing-Hui Gan, Yong-Chun Liu, Cuicui Lu, Xiao Wang, Meng Khoon Tey, and Li You. Intracavity-squeezed optomechanical cooling. *Laser & Photonics Reviews*, 13(11):1900120, 2019.

[24] Yanko Todorov, Sukhdeep Dhillon, and Juliette Mangeney. Thz quantum gap: exploring potential approaches for generating and detecting non-classical states of thz light. *Nanophotonics*, (0), 2024.

[25] Michael A Newkirk and Kerry J Vahala. Amplitude-phase decorrelation: a method for reducing intensity noise in semiconductor lasers. *IEEE journal of quantum electronics*, 27(1):13–22, 1991.

[26] J Kitching, A Yariv, and Y Shevy. Room temperature generation of amplitude squeezed light from a semiconductor laser with weak optical feedback. *Physical review letters*, 74(17):3372, 1995.

[27] F Jérémie, C Chabran, and P Gallion. Room-temperature generation of amplitude-squeezed light from 1550-nm distributed-feedback semiconductor lasers. *JOSA B*, 16(3):460–464, 1999.

[28] PD Drummond and DF Walls. Quantum theory of optical bistability. i. nonlinear polarisability model. *Journal of Physics A: Mathematical and General*, 13(2):725, 1980.

[29] Mikkel Heuck, S Combrié, G Lehoucq, S Malaguti, G Bellanca, S Trillo, Philip Trøst Kristensen, Jesper Mørk, JP Reithmaier, and A De Rossi. Heterodyne pump probe measurements of nonlinear dynamics in an indium phosphide photonic crystal cavity. *Applied Physics Letters*, 103(18):181120, 2013.

[30] Yi Yu, Evarist Palushani, Mikkel Heuck, Nadezda Kuznetsova, Philip Trøst Kristensen, Sara Ek, Dragana Vukovic, Christophe Peucheret, Leif Katsuo Oxenløwe, Sylvain Combrié, et al. Switching characteristics of an inp photonic crystal nanocavity: Experiment and theory. *Optics express*, 21(25):31047–31061, 2013.

[31] Per Lunnemann, Sara Ek, Kresten Yvind, Rozenn Piron, and Jesper Mørk. Nonlinear carrier dynamics in a quantum dash optical amplifier. *New Journal of Physics*, 14(1):013042, 2012.

[32] AA Said, Mansoor Sheik-Bahae, David J Hagan, TH Wei, J Wang, James Young, and Eric W Van Stryland. Determination of bound-electronic and free-carrier nonlinearities in znse, gaas, cdte, and znte. *JOSA B*, 9(3):405–414, 1992.

[33] Nicholas Rivera, Jamison Sloan, Yannick Salamin, John D Joannopoulos, and Marin Soljačić. Creating large fock states and massively squeezed states in optics using systems with nonlinear bound states in the continuum. *Proceedings of the National Academy of Sciences*, 120(9):e2219208120, 2023.

[34] Linh Nguyen, Jamison Sloan, Nicholas Rivera, and Marin Soljačić. Intense squeezed light from lasers with sharply nonlinear gain at optical frequencies. *Physical Review Letters*, 131(17):173801, 2023.

[35] Govind P Agrawal. *Fiber-optic communication systems*. John Wiley & Sons, 2012.

[36] Govind P Agrawal. Effect of gain and index nonlinearities on single-mode dynamics in semiconductor lasers. *IEEE journal of quantum electronics*, 26(11):1901–1909, 1990.

[37] AA Ukhanov, A Stintz, PG Eliseev, and KJ Malloy. Comparison of the carrier induced refractive index, gain, and linewidth enhancement factor in quantum dot and quantum well lasers. *Applied physics letters*, 84(7):1058–1060, 2004.

[38] Richard P Green, Ji-Hua Xu, Lukas Mahler, Alessandro Tredicucci, Fabio Beltram, Guido Giuliani, Harvey E Beere, and David A Ritchie. Linewidth enhancement factor of terahertz quantum cascade lasers. *Applied Physics Letters*, 92(7), 2008.

[39] S Machida, Y Yamamoto, and Y Itaya. Observation of amplitude squeezing in a constant-current–driven semiconductor laser. *Physical review letters*, 58(10):1000, 1987.

[40] Federico Capasso, Claire Gmachl, Roberto Paiella, Alessandro Tredicucci, Albert L Hutchinson, Deborah L Sivco, James N Baillargeon, Alfred Y Cho, and HC Liu. New frontiers in quantum cascade lasers and applications. *IEEE Journal of selected topics in quantum electronics*, 6(6):931–947, 2000.

[41] Jing Bai and DS Citrin. Intracavity nonlinearities in quantum-cascade lasers. *Journal of Applied Physics*, 106(3), 2009.

[42] Gustavo Villares, Andreas Hugi, Stéphane Blaser, and Jérôme Faist. Dual-comb spectroscopy based on quantum-cascade-laser frequency combs. *Nature communications*, 5(1):5192, 2014.

[43] C Weber, F Banit, S Butscher, A Knorr, and Andreas Wacker. Theory of the ultrafast nonlinear response of terahertz quantum cascade laser structures. *Applied physics letters*, 89(9), 2006.

[44] QY Lu, S Manna, S Slivken, DH Wu, and M Razeghi. Dispersion compensated mid-infrared quantum cascade laser frequency comb with high power output. *AIP Advances*, 7(4), 2017.

[45] Roberto Paiella, Federico Capasso, Claire Gmachl, Deborah L Sivco, James N Baillargeon, Albert L Hutchinson, Alfred Y Cho, and HC Liu. Self-mode-locking of quantum cascade lasers with giant ultrafast optical nonlinearities. *Science*, 290(5497):1739–1742, 2000.

[46] Rainer Martini, Roberto Paiella, Federico Capasso, Claire Gmachl, Harold Y Hwang, Deborah L Sivco, Alfred Y Cho, EA Whittaker, and HC Liu. Absence of relaxation oscillation in quantum cascade lasers verified by high-frequency modulation. In *Conference on Lasers and Electro-Optics*, page CPD17. Optica Publishing Group, 2001.

[47] Susumu Noda, Kyoko Kitamura, Tsuyoshi Okino, Daiki Yasuda, and Yoshinori Tanaka. Photonic-crystal surface-emitting lasers: Review and introduction of modulated-photonic crystals. *IEEE Journal of Selected Topics in Quantum Electronics*, 23(6):1–7, 2017.

[48] Chia Wei Hsu, Bo Zhen, A Douglas Stone, John D Joannopoulos, and Marin Soljačić. Bound states in the continuum. *Nature Reviews Materials*, 1(9):1–13, 2016.

[49] John E Carroll, James Whiteaway, Dick Plumb, and RGS Plumb. *Distributed feedback semiconductor lasers*, volume 10. IET, 1998.

[50] Kenichi Iga. Forty years of vertical-cavity surface-emitting laser: Invention and innovation. *Japanese Journal of Applied Physics*, 57(8S2):08PA01, 2018.

[51] Kartik Srinivasan, Matthew Borselli, Oskar Painter, Andreas Stintz, and Sanjay Krishna. Cavity q, mode volume, and lasing threshold in small diameter algaas microdisks with embedded quantum dots. *Optics express*, 14(3):1094–1105, 2006.

[52] Jesper Mork and Kresten Yvind. Squeezing of intensity noise in nanolasers and nanoleds with extreme dielectric confinement. *Optica*, 7(11):1641–1644, 2020.

[53] Sahil Pontula, Yannick Salamin, Charles Roques-Carmes, and Marin Soljacic. Multimode amplitude squeezing through cascaded nonlinear optical processes. *arXiv preprint arXiv:2405.05201*, 2024.

[54] Junaid Aasi, Joan Abadie, BP Abbott, Richard Abbott, TD Abbott, MR Abernathy, Carl Adams, Thomas Adams, Paolo Addesso, RX Adhikari, et al. Enhanced sensitivity of the ligo gravitational wave detector by using squeezed states of light. *Nature Photonics*, 7(8):613–619, 2013.

[55] R Medeiros De Araújo, Jonathan Roslund, Yin Cai, Giulia Ferrini, Claude Fabre, and Nicolas Treps. Full characterization of a highly multimode entangled state embedded in an optical frequency comb using pulse shaping. *Physical Review A*, 89(5):053828, 2014.

[56] L McCuller, C Whittle, D Ganapathy, K Komori, M Tse, A Fernandez-Galiana, L Barsotti, Peter Fritschel, M MacInnis, F Matichard, et al. Frequency-dependent squeezing for advanced ligo. *Physical review letters*, 124(17):171102, 2020.

[57] WH Louisell, A Yariv, and AE Siegman. Quantum fluctuations and noise in parametric processes. i. *Physical Review*, 124(6):1646, 1961.

[58] Jonathan Roslund, Renné Medeiros De Araujo, Shifeng Jiang, Claude Fabre, and Nicolas Treps. Wavelength-multiplexed quantum networks with ultrafast frequency combs. *Nature Photonics*, 8(2):109–112, 2014.

[59] Avik Dutt, Kevin Luke, Sasikanth Manipatruni, Alexander L Gaeta, Paulo Nussenzveig, and Michal Lipson. On-chip optical squeezing. *Physical Review Applied*, 3(4):044005, 2015.

[60] Young-Sik Ra, Adrien Dufour, Mattia Walschaers, Clément Jacquard, Thibault Michel, Claude Fabre, and Nicolas Treps. Non-gaussian quantum states of a multimode light field. *Nature Physics*, 16(2):144–147, 2020.

[61] Yun Zhao, Yoshitomo Okawachi, Jae K Jang, Xingchen Ji, Michal Lipson, and Alexander L Gaeta. Near-degenerate quadrature-squeezed vacuum generation on a silicon-nitride chip. *Physical Review Letters*, 124(19):193601, 2020.

[62] Varun D Vaidya, B Morrison, LG Helt, R Shahrokshahi, DH Mahler, MJ Collins, K Tan, J Lavoie, A Repingon, M Menotti, et al. Broadband quadrature-squeezed vacuum and nonclassical photon number correlations from a nanophotonic device. *Science advances*, 6(39):eaba9186, 2020.

[63] Zijiao Yang, Mandana Jahanbozorgi, Dongin Jeong, Shuman Sun, Olivier Pfister, Hansuek Lee, and Xu Yi. A squeezed quantum microcomb on a chip. *Nature Communications*, 12(1):4781, 2021.

[64] Melissa A Guidry, Daniil M Lukin, Ki Youl Yang, and Jelena Vučković. Multimode squeezing in soliton crystal microcombs. *Optica*, 10(6):694–701, 2023.

[65] Federico Presutti, Logan G Wright, Shi-Yuan Ma, Tianyu Wang, Benjamin K Malia, Tatsuhiro Onodera, and Peter L McMahon. Highly multimode visible squeezed light with programmable spectral correlations through broadband upconversion. *arXiv preprint arXiv:2401.06119*, 2024.

[66] Hubert S Stokowski, Devin J Dean, Alexander Y Hwang, Taewon Park, Oguz Tolga Celik, Timothy P McKenna, Marc Jankowski, Carsten Langrock, Vahid Ansari, Martin M Fejer, et al. Integrated frequency-modulated optical parametric oscillator. *Nature*, 627(8002):95–100, 2024.

[67] Marc Jankowski, Ryotatsu Yanagimoto, Edwin Ng, Ryan Hamerly, Timothy P McKenna, Hideo Mabuchi, and MM Fejer. Ultrafast second-order nonlinear photonics–from classical physics to non-gaussian quantum dynamics. *arXiv preprint arXiv:2401.06265*, 2024.

[68] Claude Fabre, E Giacobino, Antoine Heidmann, and Serge Reynaud. Noise characteristics of a non-degenerate optical parametric oscillator-application to quantum noise reduction. *Journal de Physique*, 50(10):1209–1225, 1989.

[69] J Mertz, A Heidmann, C Fabre, E Giacobino, and S Reynaud. Observation of high-intensity sub-poissonian light using an optical parametric oscillator. *Physical review letters*, 64(24):2897, 1990.

[70] JU Fürst, DV Strekalov, D Elser, A Aiello, Ulrik Lund Andersen, Ch Marquardt, and G Leuchs. Quantum light from a whispering-gallery-mode disk resonator. *Physical review letters*, 106(11):113901, 2011.

[71] Claude Fabre and Nicolas Treps. Modes and states in quantum optics. *Reviews of Modern Physics*, 92(3):035005, 2020.

[72] Ian B Burgess, Alejandro W Rodriguez, Murray W McCutcheon, Jorge Bravo-Abad, Yinan Zhang, Steven G Johnson, and Marko Lončar. Difference-frequency generation with quantum-limited efficiency in triply-resonant nonlinear cavities. *Optics express*, 17(11):9241–9251, 2009.

[73] Koustuban Ravi, Michael Hemmer, Giovanni Cirmi, Fabian Reichert, Damian N Schimpf, Oliver D Mücke, and Franz X Kärtner. Cascaded parametric amplification for highly efficient terahertz generation. *Optics letters*, 41(16):3806–3809, 2016.

[74] Michael Hemmer, G Cirmi, K Ravi, Fabian Reichert, F Ahr, L Zapata, OD Mücke, A-L Calendron, H Çankaya, D Schimpf, et al. Cascaded interactions mediated by terahertz radiation. *Optics express*, 26(10):12536–12546, 2018.

[75] Yaowen Hu, Mengjie Yu, Neil Sinclair, Di Zhu, Rebecca Cheng, Cheng Wang, and Marko Lončar. Mirror-induced reflection in the frequency domain. *Nature Communications*, 13(1):6293, 2022.

[76] Yannick Salamin, Charles Roques-Carmes, Zin Lin, Steven G Johnson, and Marin Soljačić. Overcoming the manley-rowe limit for cw terahertz generation in q-engineered multimodal cavity. In *CLEO: QELS_ Fundamental Science*, pages FTu2J–3. Optica Publishing Group, 2021.

[77] Shayan Mookherjea and Amnon Yariv. Coupled resonator optical waveguides. *IEEE Journal of selected topics in quantum electronics*, 8(3):448–456, 2002.

[78] Nicholas Rivera, Jamison Sloan, Yannick Salamin, John D Joannopoulos, and Marin Soljačić. Creating large fock states and massively squeezed states in optics using systems with nonlinear bound states in the continuum. *Proceedings of the National Academy of Sciences*, 120(9):e2219208120, 2023.

[79] Robert W Boyd, Alexander L Gaeta, and Enno Giese. Nonlinear optics. In *Springer Handbook of Atomic, Molecular, and Optical Physics*, pages 1097–1110. Springer, 2008.

[80] Shiekh Zia Uddin, Nicholas Rivera, Devin Seyler, Yannick Salamin, Jamison Sloan, Charles Roques-Carmes, Shutao Xu, Michelle Sander, and Marin Soljacic. An ab initio framework for understanding and controlling quantum fluctuations in highly multimoded light-matter systems. *arXiv preprint arXiv:2311.05535*, 2023.

[81] Wei Qin, Adam Miranowicz, Peng-Bo Li, Xin-You Lü, Jian-Qiang You, and Franco Nori. Exponentially enhanced light-matter interaction, cooperativities, and steady-state entanglement using parametric amplification. *Physical Review Letters*, 120(9):093601, 2018.

[82] Sina Zeytinoğlu, Ataç İmamoğlu, and Sebastian Huber. Engineering matter interactions using squeezed vacuum. *Physical Review X*, 7(2):021041, 2017.

[83] Shaun C Burd, Raghavendra Srinivas, Hannah M Knaack, Wenchao Ge, Andrew C Wilson, David J Wineland, Dietrich Leibfried, John J Bollinger, DTC Allcock, and DH Slichter. Quantum amplification of boson-mediated interactions. *Nature Physics*, 17(8):898–902, 2021.

[84] C Leroux, LCG Govia, and AA Clerk. Enhancing cavity quantum electrodynamics via antisqueezing: Synthetic ultrastrong coupling. *Physical review letters*, 120(9):093602, 2018.

[85] Varun D Vaidya, Yudan Guo, Ronen M Kroeze, Kyle E Ballantine, Alicia J Kollár, Jonathan Keeling, and Benjamin L Lev. Tunable-range, photon-mediated atomic interactions in multimode cavity qed. *Physical Review X*, 8(1):011002, 2018.

[86] Luqi Yuan, Qian Lin, Meng Xiao, and Shanhui Fan. Synthetic dimension in photonics. *Optica*, 5(11):1396–1405, 2018.

[87] Eran Lustig and Mordechai Segev. Topological photonics in synthetic dimensions. *Advances in Optics and Photonics*, 13(2):426–461, 2021.

[88] Arkadev Roy, Saman Jahani, Qiushi Guo, Avik Dutt, Shanhui Fan, Mohammad-Ali Miri, and Alireza Marandi. Nondissipative non-hermitian dynamics and exceptional points in coupled optical parametric oscillators. *Optica*, 8(3):415–421, 2021.

[89] Kai Wang, Avik Dutt, Ki Youl Yang, Casey C Wojcik, Jelena Vučković, and Shanhui Fan. Generating arbitrary topological windings of a non-hermitian band. *Science*, 371(6535):1240–1245, 2021.

[90] Luqi Yuan, Avik Dutt, and Shanhui Fan. Synthetic frequency dimensions in dynamically modulated ring resonators. *APL Photonics*, 6(7), 2021.

[91] Luis Ledezma, Arkadev Roy, Luis Costa, Ryoto Sekine, Robert Gray, Qiushi Guo, Rajveer Nehra, Ryan M Briggs, and Alireza Marandi. Octave-spanning

tunable infrared parametric oscillators in nanophotonics. *Science Advances*, 9(30):eadf9711, 2023.

[92] Jintian Lin, Yingxin Xu, Zhiwei Fang, Min Wang, Jiangxin Song, Nengwen Wang, Lingling Qiao, Wei Fang, and Ya Cheng. Fabrication of high-q lithium niobate microresonators using femtosecond laser micromachining. *Scientific reports*, 5(1):8072, 2015.

[93] ZhenZhong Hao, Li Zhang, Ang Gao, WenBo Mao, XiaoDan Lyu, XiaoMei Gao, Fang Bo, Feng Gao, GuoQuan Zhang, and JingJun Xu. Periodically poled lithium niobate whispering gallery mode microcavities on a chip. *Science China Physics, Mechanics & Astronomy*, 61:1–5, 2018.

[94] Y Yamamoto, N Imoto, and S Machida. Amplitude squeezing in a semiconductor laser using quantum nondemolition measurement and negative feedback. *Physical Review A*, 33(5):3243, 1986.

[95] Robert W Boyd. *Nonlinear optics*. Academic press, 2020.

[96] Luigi R Brovelli and Ursula Keller. Simple analytical expressions for the reflectivity and the penetration depth of a bragg mirror between arbitrary media. *Optics communications*, 116(4-6):343–350, 1995.

[97] HW Yen, W Ng, I Samid, and A Yariv. Gaas distributed bragg reflector lasers. *Optics Communications*, 17(3):213–218, 1976.

[98] YOSHIHISA Yamamoto and NOBUYUKI Imoto. Internal and external field fluctuations of a laser oscillator: Part i–quantum mechanical langevin treatment. *IEEE journal of quantum electronics*, 22(10):2032–2042, 1986.

[99] Tobias Gensty, Wolfgang Elsäßer, and Christian Mann. Intensity noise properties of quantum cascade lasers. *Optics Express*, 13(6):2032–2039, 2005.